

Continuous-Aperture Array-Based ISAC Over Fading Channels

Boqun Zhao, *Graduate Student Member, IEEE*, Chongjun Ouyang, *Member, IEEE*,
Xingqi Zhang, *Senior Member, IEEE*, and Yuanwei Liu, *Fellow, IEEE*

Abstract—A framework of continuous-aperture array (CAPA)-based integrated sensing and communications (ISAC) under a fading communication channel is proposed. A continuous operator-based signal model is developed, and the statistics of the communication channel gain are characterized via Landau’s eigenvalue theorem. On this basis, the performance of the CAPA-based ISAC system is analyzed by considering three continuous beamforming designs: i) the sensing-centric (S-C) design that optimizes sensing performance, ii) the communication-centric (C-C) design that optimizes communication performance, and iii) the Pareto-optimal design that balances the sensing-communication trade-off. For the S-C and C-C design, closed-form expressions for the sensing rate (SR), ergodic communication rate (CR), and outage probability are derived, and high-signal-to-noise ratio asymptotic analysis is conducted to obtain the multiplexing and diversity gains. For the Pareto-optimal design, the Pareto-optimal beamformer achieving the Pareto boundary is derived, and the achievable SR-CR region is characterized. Numerical results demonstrate that the proposed CAPA-ISAC scheme outperforms both conventional spatially discrete arrays-based ISAC and CAPA-based frequency-division sensing and communications.

Index Terms—Continuous-aperture array (CAPA), fading channels, integrated sensing and communications (ISAC), Pareto optimality, performance analysis.

I. INTRODUCTION

Integrated sensing and communications (ISAC) has emerged as a key enabler for future wireless networks, driven by the need to reuse spectrum and hardware while supporting perception-centric applications such as localization, tracking, and environment mapping [1]. By allowing sensing and communications to share waveform, spectrum, and infrastructure, ISAC promises improved resource efficiency and new system-level synergies, but also introduces intrinsic conflicts between the two functionalities in waveform/beamforming design and performance evaluation. A growing body of work has therefore focused on establishing performance metrics, fundamental trade-offs, and design principles for dual-functional systems, ranging from information-theoretic formulations to signal processing-oriented transceiver optimization [1], [2]. In particular, mutual-information (MI)-based metrics provide a unified way to quantify both sensing and communication capabilities and to characterize their trade-off under a common information measure [3], [4].

B. Zhao and X. Zhang are with the Department of Electrical and Computer Engineering, University of Alberta, Edmonton AB, T6G 2R3, Canada (email: {boqun1, xingqi.zhang}@ualberta.ca).

C. Ouyang is with the School of Electronic Engineering and Computer Science, Queen Mary University of London, London, E1 4NS, U.K. (e-mail: c.ouyang@qmul.ac.uk).

Y. Liu is with the Department of Electrical and Electronic Engineering, The University of Hong Kong, Hong Kong (e-mail: yuanwei@hku.hk).

In parallel, continuous-aperture array (CAPA) architectures have gained increasing attention as an electromagnetic (EM)-consistent abstraction for antenna systems, where the radiating structure is modeled via a continuous current distribution over a spatial aperture [5]. This continuous viewpoint changes both modeling and optimization: instead of finite-dimensional beamforming vectors used in spatially discrete arrays (SP-DAs), CAPA transmit/receive processing is more naturally described as functional beamforming defined over a continuous spatial domain. Consequently, the fundamental spatial dimensionality is governed by signal-space arguments and the spectral properties of aperture-domain operators, which connect CAPA performance limits to spatial degrees of freedom (DoFs) characterized by operator spectra and spatial bandwidth notions [6]–[8]. This operator-based perspective also opens the door to analyzing CAPA systems under physically grounded stochastic channel models, where the channel can be represented as an EM random field [9]. These features make CAPA a natural candidate for ISAC, where fine spatial focusing and controllable beampatterns are highly valuable for both communication coverage and sensing resolution.

A. Prior Works

ISAC has been extensively studied in terms of waveform/precoder design, performance trade-offs, and system architectures, as summarized in major surveys and tutorials [1], [2]. In particular, MI-based sensing has been used to establish information-theoretic limits and to connect sensing quality directly to waveform/beamformer design under a unified information measure [3], [4]. These studies provide important foundations for joint design, but many of them adopt finite-dimensional discrete-array models, which can not directly carry over to continuous-aperture architectures.

Recent studies on CAPAs establish EM-consistent channel models and continuous-domain transmission frameworks in which beamforming becomes a functional design and performance is governed by the spectra of spatial correlation operators. In particular, fundamental-limit work on continuous-aperture surfaces provides useful physical insights and DoF-type interpretations that motivate continuous-domain formulations [8], [10]. Further, EM-consistent random channel characterizations provide a principled statistical basis for continuous-aperture links and naturally lead to operator-based correlation descriptions [9]. Building on these foundations, capacities for CAPA communications have been characterized using operator-based formulations [11], and multipath-induced spatial fading models and associated performance metrics (e.g.,

diversity and multiplexing gains) have also been investigated [12]. Moreover, a growing body of work studies CAPA beamforming optimization. However, these works provide useful tools solely for CAPA-based communications [13]–[18] or sensing [19]–[21], but do not directly resolve the coupled sensing–communication design.

B. Motivations and Contributions

Initial CAPA-ISAC works have started to characterize the system performance and investigate sensing-communications trade-offs in the continuous-aperture setting [22], [23]. However, existing CAPA-ISAC studies predominantly consider deterministic line-of-sight (LoS) channels, which may be overly idealised and not reflect practical conditions. In contrast, CAPA-ISAC over fading channels remains largely unexplored. In realistic environments, multipath scattering and small-scale fading are ubiquitous and can fundamentally affect reliability (outage) and average performance (ergodic rate). Therefore, there remains a clear need for a unified and tractable analytical framework for CAPA-based ISAC over fading channels.

However, the extension from LoS to non-LoS models is nontrivial because it requires handling operator-based random channels. Moreover, EM randomness induced by scattering makes performance evaluation analytically challenging. In particular, under multipath scattering, the effective channel gain becomes a functional of a correlated continuous random field over the aperture, for which a closed-form distribution is generally unavailable. This prevents rigorous derivation of performance metrics, e.g., ergodic communication rate (ECR) and outage probability (OP), and tractable sensing–communication trade-off characterizations for CAPA-ISAC.

Motivated by the above gaps and challenges, this paper develops a unified modeling and analysis framework for CAPA-based ISAC. Specifically, the sensing link is modeled via spherical-wave propagation and a Swerling-I radar cross-section (RCS) model, while the communication link is modeled as an EM multipath channel induced by scatterers, leading to a continuous random-field representation over the transmit aperture. Our main contributions are summarized as follows:

- We establish a continuous-aperture signal model for dual-functional sensing and communications (DFSAC) transmission where the beamformer is a normalized source-current field over the transmit aperture. MI-based sensing and communication performance metrics, i.e., sensing rate (SR) and communication (CR), are explicitly expressed as functionals of the continuous beamformer.
- By characterizing the autocorrelation structure of the aperture-domain fading channel, we connect the eigenvalue behaviour of the induced sinc kernel operator to the effective spatial DoFs. Using Landau’s eigenvalue theorem, we show an eigenvalue “polarization” phenomenon governed by DoFs, which enables accurate finite-sum approximations for the continuous channel gain distribution. This yields an analytically tractable pathway to evaluate ergodic and outage metrics in CAPA fading channels.
- We investigate two continuous beamforming strategies: the sensing-centric (S-C) design that maximizes sensing

rate (SR), and the communication-centric (C-C) design that maximizes communication rate (CR). For each design, we derive closed-form expressions for SR, ECR, and OP, together with high-SNR asymptotic results that explicitly reveal the high-SNR slopes and diversity orders. Further, to quantify the sensing–communication trade-off, we formulate the Pareto boundary characterization problem for the achievable SR–CR region. By using a subspace method, we convert the intractable functional optimization into a low-dimensional vector optimization, from which a closed-form Pareto-optimal beamformer is obtained.

- Numerical results validate the derived expressions and show that CAPA-ISAC can strictly enlarge the achievable SR–CR region compared with conventional SPDA-based ISAC and CAPA-based frequency-division sensing and communications (FDSAC). The results further highlight the role of effective DoFs in explaining the observed diversity advantages, and it is shown that the benefits of aperture enlargement depend critically on beamformer alignment with the target metric, thereby motivating the proposed Pareto trade-off design.

C. Organization and Notations

The remainder of this paper is organized as follows. Section II introduces the CAPA-ISAC system model, including the sensing and communication signal models and the corresponding metrics. Section III characterizes the statistical properties of the fading communication channel and derives the probability density function (PDF) of the channel gain. Section IV presents the performance analysis under the S-C, C-C, and Pareto-optimal beamforming designs, including closed-form SR/ECR/OP expressions and multiplexing/diversity characterizations. Section V provides numerical results and comparisons with SPDA-ISAC and CAPA-FDSAC baselines. Section VI concludes the paper.

Notations: Throughout this paper, scalars, vectors, and matrices are denoted by non-bold, bold lower-case, and bold upper-case letters, respectively. For the matrix \mathbf{A} , \mathbf{A}^T , \mathbf{A}^* and \mathbf{A}^H denote its transpose, conjugate, and conjugate transpose, respectively. The notations $|a|$ and $\|\mathbf{a}\|$ denote the magnitude and norm of scalar a and vector \mathbf{a} , respectively. The identity matrix with dimensions $N \times N$ is represented by \mathbf{I}_N . The set \mathbb{R} and \mathbb{C} stand for the real and complex spaces, respectively, and notation $\mathbb{E}\{\cdot\}$ represents mathematical expectation. The MI between random variables X and Y conditioned on Z is shown by $I(X; Y|Z)$. Finally, $\mathcal{CN}(\boldsymbol{\mu}, \mathbf{X})$ is used to denote the circularly-symmetric complex Gaussian distribution with mean $\boldsymbol{\mu}$ and covariance matrix \mathbf{X} , and $\text{Exp}(\lambda)$ represents the exponential distribution with rate parameter λ .

II. SYSTEM MODEL

A. System Description

We consider a downlink CAPA-based ISAC system, where a DFSAC base station (BS) sends data to a single-antenna CU while simultaneously sensing a point-like target. As illustrated in Fig. 1, the BS is equipped with two uni-polarized linear

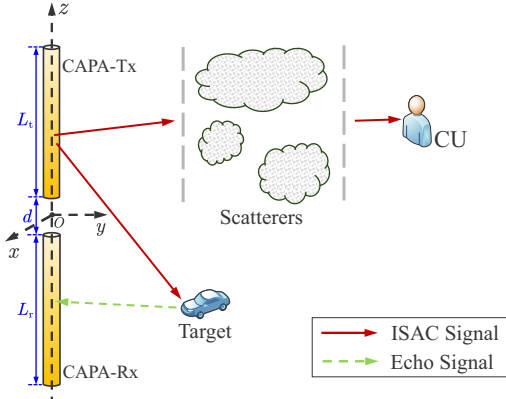


Fig. 1: Illustration of CAPA-based ISAC.

CAPAs: a transmit CAPA with a length of L_t and a receive CAPA with a physical length of L_r . The CAPAs are positioned along the z -axis, separated end-to-end by a distance d , and the midpoint of this distance is defined as the origin. Therefore, the apertures of the transmit and receive CAPAs are, respectively, given by

$$\mathcal{A}_t = \{[0, 0, z]^T | z \in [d/2, d/2 + L_t]\}, \quad (1a)$$

$$\mathcal{A}_r = \{[0, 0, z]^T | z \in [-d/2 - L_r, -d/2]\}. \quad (1b)$$

Let $\mathbf{x}(\mathbf{t}) = [x_1(\mathbf{t}), \dots, x_L(\mathbf{t})] \in \mathbb{C}^{1 \times L}$ represent the DFSAC signal emitted by the transmit CAPA at $\mathbf{t} \in \mathcal{A}_t$, where L denotes the number of symbols in a communication frame or the count of sensing pulses. Within the communication context, each $x_\ell(\mathbf{t})$ corresponds to the ℓ th transmitted symbol, for $\ell = 1, \dots, L$. In the sensing scenario, $x_\ell(\mathbf{t})$ indicates the sensing snapshot transmitted at the ℓ th time interval.

In the CAPA-ISAC framework, the continuous DFSAC signal is constructed as follows:

$$\mathbf{x}(\mathbf{t}) = \sqrt{P}w(\mathbf{t})\mathbf{s}^T, \quad (2)$$

where P is the transmit power, $\mathbf{s} \in \mathbb{C}^{L \times 1}$ is a unit-power data stream intended for the CU, and $w(\mathbf{t})$ denotes the normalized source current or transmit beamformer. $w(\cdot)$ is a scalar field over $\mathbb{R}^{3 \times 1}$, and the beamformer satisfies the energy constraint:

$$\int_{\mathcal{A}_t} |w(\mathbf{t})|^2 d\mathbf{t} = 1. \quad (3)$$

Here, $w(\mathbf{t})$ maps each spatial point \mathbf{t} on the transmitting array to a complex scalar. The data vector $\mathbf{s} = [s_1, \dots, s_L]^T$ fulfills the condition $\frac{1}{L}|\mathbf{s}|^2 = 1$, where each s_ℓ represents a modulated symbol sent at the ℓ th interval. Consequently, the transmitted signal at time index ℓ becomes

$$x_\ell(\mathbf{t}) = \sqrt{P}s_\ell w(\mathbf{t}), \quad \ell = 1, \dots, L. \quad (4)$$

B. Sensing Model

At the ℓ th time interval, the received echo signal at the BS at point $\mathbf{r} \in \mathcal{A}_r$ for target sensing can be written as follows:

$$y_{s,\ell}(\mathbf{r}) = \int_{\mathcal{A}_t} q(\mathbf{r}, \mathbf{t})x_\ell(\mathbf{t})d\mathbf{t} + n_{s,\ell}(\mathbf{r}), \quad (5)$$

where $y_{s,\ell}(\cdot)$ is the receive vector field, $q(\cdot, \cdot)$ is a complex integral kernel denoting the sensing response, and $n_{s,\ell}(\cdot)$ represents thermal noise. The term $q(\mathbf{r}, \mathbf{t})$ gives the sensing

response between the transmit position $\mathbf{t} \in \mathcal{A}_t$ and the receive position $\mathbf{r} \in \mathcal{A}_r$. The noise field is characterized as a zero-mean complex Gaussian random process, satisfying

$$\mathbb{E}\{n_{s,\ell}(\mathbf{r})n_{s,\ell}^*(\mathbf{r}')\} = \sigma_s^2\delta(\mathbf{r} - \mathbf{r}'), \quad (6)$$

where $\delta(\cdot)$ is the Dirac delta function, and σ_s^2 is the power spectral density of the noise. It is also assumed that the transmitted symbol sequence \mathbf{s} and the noise fields $\{n_{s,\ell}(\mathbf{r})\}_{\ell=1}^L$ are statistically independent.

The sensing response can be modeled as follows [9]:

$$q(\mathbf{r}, \mathbf{t}) = \int h_s(\mathbf{r}, \mathbf{p})a(\mathbf{p})h_s(\mathbf{p}, \mathbf{t})d\mathbf{p}, \quad (7)$$

where $h_s(\mathbf{x}, \mathbf{y})$ denotes the sensing link between points \mathbf{x} and \mathbf{y} , and $a(\mathbf{p})$ corresponds to the scattering coefficient or reflectivity, commonly referred to as the RCS, at point \mathbf{p} . To precisely capture the characteristics of the LoS sensing links in both near-field and far-field scenarios, we model the sensing links based on the non-uniform spherical-wave propagation as follows [24]:

$$h_s(\mathbf{x}, \mathbf{y}) = \frac{e^{-jk_0\|\mathbf{x}-\mathbf{y}\|}}{\sqrt{4\pi\|\mathbf{x}-\mathbf{y}\|}}, \quad (8)$$

where $k_0 = \frac{2\pi}{\lambda}$ with λ being the wavelength denotes the wavenumber.

Based on the ray-tracing model in [25], the scattering response can be expressed as follows:

$$a(\mathbf{p}) = \sum_{n=1}^N \beta_n \delta(\mathbf{p} - \mathbf{p}_n), \quad (9)$$

where N is the number of resolvable point-like targets, $\mathbf{p}_n \in \mathbb{R}^{3 \times 1}$ represents the location of the n th target, and β_n denotes the associated RCS. In this work, we consider a single point-like target, i.e., $N = 1$, located at

$$\mathbf{p}_s = [p_{s,x}, p_{s,y}, p_{s,z}]^T, \quad (10)$$

with an RCS of β_s . Consequently, the scattering response reduces to

$$a(\mathbf{p}) = \beta_s \delta(\mathbf{p} - \mathbf{p}_s). \quad (11)$$

Substituting into (7), the response becomes:

$$q(\mathbf{r}, \mathbf{t}) = h_s(\mathbf{r}, \mathbf{p}_s)\beta_s h_s(\mathbf{p}_s, \mathbf{t}). \quad (12)$$

For notational simplicity, we denote $h_s(\mathbf{p}_s, \mathbf{t}) \triangleq h_s(\mathbf{t})$ for $\mathbf{t} \in \mathcal{A}_t$ and $h_s(\mathbf{r}, \mathbf{p}_s) \triangleq h_s(\mathbf{r})$ for $\mathbf{r} \in \mathcal{A}_r$. Accordingly, the received echo signal at point \mathbf{r} can be expressed as follows:

$$y_{s,\ell}(\mathbf{r}) = h_s(\mathbf{r})\beta_s \int_{\mathcal{A}_t} h_s(\mathbf{t})x_\ell(\mathbf{t})d\mathbf{t} + n_{s,\ell}(\mathbf{r}). \quad (13)$$

Following the Swerling-I model [26], the RCS β_s is considered stable across different pulses and is characterized by a Rayleigh-distributed magnitude. Consequently, β_s is modeled as a circularly symmetric complex Gaussian random variable, i.e., $\beta_s \sim \mathcal{CN}(0, \alpha_s)$, where $\alpha_s > 0$ denotes the mean power of the RCS. This quantity reflects the average strength of the target's reflectivity [26].

This study assumes that the target's position is accurately known, allowing us to concentrate on estimating its RCS β_s . In this context, the objective of sensing is to retrieve environmental information encoded in β_s from the observed echo signals $\{y_{s,\ell}(\mathbf{r})\}_{\ell=1}^L$, utilizing prior knowledge of the

transmitted signal $\mathbf{x}(\mathbf{t})$. To this end, the receiver employs a detector $v_s(\mathbf{r})$ for $\mathbf{r} \in \mathcal{A}_r$, which yields

$$\int_{\mathcal{A}_r} v_s^*(\mathbf{r}) y_{s,\ell}(\mathbf{r}) d\mathbf{r} = \sqrt{P} s_\ell \beta_s \int_{\mathcal{A}_r} v_s^*(\mathbf{r}) h_s(\mathbf{r}) d\mathbf{r} \times \int_{\mathcal{A}_t} h_s(\mathbf{t}) w(\mathbf{t}) d\mathbf{t} + \int_{\mathcal{A}_r} v_s^*(\mathbf{r}) n_{s,\ell}(\mathbf{r}) d\mathbf{r}. \quad (14)$$

For clarity, we denote $\hat{y}_{s,\ell} \triangleq \int_{\mathcal{A}_r} v_s^*(\mathbf{r}) y_{s,\ell}(\mathbf{r}) d\mathbf{r}$, $\hat{h}_r \triangleq \int_{\mathcal{A}_r} v_s^*(\mathbf{r}) h_s(\mathbf{r}) d\mathbf{r}$, $\hat{h}_t \triangleq \int_{\mathcal{A}_t} h_s(\mathbf{t}) w(\mathbf{t}) d\mathbf{t}$, and $\hat{n}_{s,\ell} \triangleq \int_{\mathcal{A}_r} v_s^*(\mathbf{r}) n_{s,\ell}(\mathbf{r}) d\mathbf{r}$. As per [11, Lemma 1], we have $\hat{n}_{s,\ell} \sim \mathcal{CN}(0, \sigma_s^2 \int_{\mathcal{A}_r} |v_s(\mathbf{r})|^2 d\mathbf{r})$. Hence, (14) can be rewritten as follows:

$$\hat{y}_{s,\ell} = \sqrt{P} \hat{h}_r \beta_s \hat{h}_t s_\ell + \hat{n}_{s,\ell}, \quad \ell = 1, \dots, L, \quad (15)$$

which yields

$$\hat{\mathbf{y}}_s = \sqrt{P} \hat{h}_r \hat{h}_t \mathbf{s} \beta_s + \hat{\mathbf{n}}_s, \quad (16)$$

where $\hat{\mathbf{y}}_s = [\hat{y}_{s,1}, \dots, \hat{y}_{s,L}]^\top \in \mathbb{C}^{L \times 1}$ and $\hat{\mathbf{n}}_s = [\hat{n}_{s,1}, \dots, \hat{n}_{s,L}]^\top \sim \mathcal{CN}(\mathbf{0}, \sigma_s^2 \int_{\mathcal{A}_r} |v_s(\mathbf{r})|^2 d\mathbf{r} \mathbf{I}_L)$.

The next task is to recover β_s from $\hat{\mathbf{y}}_s$ given \mathbf{s} . The information-theoretic limits of sensing performance is characterized by the sensing MI, which quantifies how much information about β_s is contained in $\hat{\mathbf{y}}_s$ when conditioned on \mathbf{s} [3]. To assess performance, we adopt the SR as the performance metric, which is defined as the sensing MI per unit time. Notably, under our considered model, a larger SR also implies a smaller mean-squared error and Bayesian Cramér-Rao bound [4], [22]. Since each DFSAC symbol lasts one unit of time, the SR can be written as follows:

$$\mathcal{R}_s(w(\mathbf{t})) = \frac{1}{L} I(\hat{\mathbf{y}}_s; \beta_s | \mathbf{s}), \quad (17)$$

where $I(\hat{\mathbf{y}}_s; \beta_s | \mathbf{s})$ denotes the sensing MI. Viewing the model in (16) as a virtual single-input multiple-output channel, we interpret β_s as the input, $\hat{\mathbf{y}}_s$ as the output, and $\hat{h}_r \hat{h}_t \mathbf{s}$ as the effective channel gain, with an additive noise $\hat{\mathbf{n}}_s$. The resulting MI is equivalent to the capacity of this virtual MISO channel, computed as

$$I(\hat{\mathbf{y}}_s; \beta_s | \mathbf{s}) = \log_2 \det \left(\mathbf{I}_L + \frac{P \alpha_s |\hat{h}_r|^2 |\hat{h}_t|^2}{\sigma_s^2 \int_{\mathcal{A}_r} |v_s(\mathbf{r})|^2 d\mathbf{r}} \mathbf{s} \mathbf{s}^H \right) = \log_2 \left(1 + \frac{P \alpha_s |\hat{h}_r|^2 |\hat{h}_t|^2}{\sigma_s^2 \int_{\mathcal{A}_r} |v_s(\mathbf{r})|^2 d\mathbf{r}} \|\mathbf{s}\|^2 \right), \quad (18)$$

where the second equality results from applying Sylvester's determinant identity. Substituting (18) into (17) and using $\frac{1}{L} \|\mathbf{s}\|^2 = 1$, the SR can be expressed as follows:

$$\mathcal{R}_s(w(\mathbf{t})) = \frac{1}{L} \log_2 \left(1 + \frac{P \alpha_s |\hat{h}_r|^2 |\hat{h}_t|^2}{\sigma_s^2 \int_{\mathcal{A}_r} |v_s(\mathbf{r})|^2 d\mathbf{r}} L \right). \quad (19)$$

Here, SR is influenced by the choice of detector $v_s(\mathbf{r})$. To maximize the SR, we solve the following optimization problem:

$$\max_{v_s(\mathbf{r})} \frac{|\hat{h}_r|^2}{\int_{\mathcal{A}_r} |v_s(\mathbf{r})|^2 d\mathbf{r}} \Leftrightarrow \max_{v_s(\mathbf{r})} \frac{\left| \int_{\mathcal{A}_r} v_s^*(\mathbf{r}) h_s(\mathbf{r}) d\mathbf{r} \right|^2}{\int_{\mathcal{A}_r} |v_s(\mathbf{r})|^2 d\mathbf{r}}. \quad (20)$$

The optimal solution occurs when $v_s(\mathbf{r})$ is proportional to

$h_s(\mathbf{r})$, i.e., $v_s(\mathbf{r}) \propto h_s(\mathbf{r})$, which gives

$$\max_{v_s(\mathbf{r})} \frac{|\hat{h}_r|^2}{\int_{\mathcal{A}_r} |v_s(\mathbf{r})|^2 d\mathbf{r}} = \frac{\left| \int_{\mathcal{A}_r} h_s(\mathbf{r}) d\mathbf{r} \right|^2}{\int_{\mathcal{A}_r} |h_s(\mathbf{r})|^2 d\mathbf{r}} = \int_{\mathcal{A}_r} |h_s(\mathbf{r})|^2 d\mathbf{r}. \quad (21)$$

Finally, substituting (21) back into (19) yields

$$\mathcal{R}_s(w(\mathbf{t})) = \frac{1}{L} \log_2 \left(1 + \bar{\gamma}_s L \alpha_s \int_{\mathcal{A}_r} |h_s(\mathbf{r})|^2 d\mathbf{r} \times \left| \int_{\mathcal{A}_t} h_s(\mathbf{t}) w(\mathbf{t}) d\mathbf{t} \right|^2 \right), \quad (22)$$

where $\bar{\gamma}_s \triangleq \frac{P}{\sigma_s^2}$.

C. Communication Model

At the ℓ th time interval, the received signal at the CU is given by

$$y_{c,\ell} = \int_{\mathcal{A}_t} h_c(\mathbf{p}_c, \mathbf{t}) x_\ell(\mathbf{t}) d\mathbf{t} + n_{c,\ell}, \quad (23)$$

for $\ell = 1, \dots, L$, where \mathbf{p}_c is the position of the CU, $h_c(\mathbf{p}_c, \mathbf{t})$ represents the spatial response from $\mathbf{t} \in \mathcal{A}_t$ to the CU, and $n_{c,\ell} \sim \mathcal{CN}(0, \sigma_c^2)$ represents the additive noise.

We consider a scenario in which no direct path exists between the transmit CAPA and the CU due to the presence of scatterers. In this case, the EM multipath spatial response, $h_c(\mathbf{p}_c, \mathbf{t}) \triangleq h_c(\mathbf{t})$, can be modeled as follows [9]:

$$h_c(\mathbf{t}) = \frac{1}{(2\pi)^2} \iiint_{\mathcal{D}(\mathbf{k}) \times \mathcal{D}(\boldsymbol{\kappa})} e^{-j\mathbf{k}^\top \mathbf{p}_c} H(\mathbf{k}, \boldsymbol{\kappa}) e^{j\boldsymbol{\kappa}^\top \mathbf{t}} d\mathbf{k} d\boldsymbol{\kappa}, \quad (24)$$

where $\mathbf{k} = [k_x, \gamma(k_x, k_z), k_z]^\top \in \mathbb{R}^{3 \times 1}$, $\boldsymbol{\kappa} = [\kappa_x, \gamma(\kappa_x, \kappa_z), \kappa_z]^\top \in \mathbb{R}^{3 \times 1}$, $\gamma(x, y) = \sqrt{k_0^2 - x^2 - y^2}$, $\mathcal{D}(\mathbf{k}) = \{(k_x, k_z) | k_x^2 + k_z^2 \leq k_0^2\}$, and $\mathcal{D}(\boldsymbol{\kappa}) = \{(\kappa_x, \kappa_z) | \kappa_x^2 + \kappa_z^2 \leq \kappa_0^2\}$. In particular, $e^{j\boldsymbol{\kappa}^\top \mathbf{t}}$ and $e^{-j\mathbf{k}^\top \mathbf{p}_c}$ denote the transmit and receive plane waves propagating in directions $\frac{\boldsymbol{\kappa}}{\|\boldsymbol{\kappa}\|}$ and $\frac{\mathbf{k}}{\|\mathbf{k}\|}$, respectively, and $H(\mathbf{k}, \boldsymbol{\kappa})$ represents the angular response that maps the transmit direction $\frac{\boldsymbol{\kappa}}{\|\boldsymbol{\kappa}\|}$ to the receive direction $\frac{\mathbf{k}}{\|\mathbf{k}\|}$. For analytical tractability, by considering the isotropic scattering, $H(\mathbf{k}, \boldsymbol{\kappa})$ is modeled as a stationary, circularly symmetric, complex-Gaussian random field, which yields

$$H(\mathbf{k}, \boldsymbol{\kappa}) = \frac{A_s(k_0)}{\sqrt{\gamma(k_x, k_z) \gamma(\kappa_x, \kappa_z)}} W(\mathbf{k}, \boldsymbol{\kappa}). \quad (25)$$

Here, $W(\mathbf{k}, \boldsymbol{\kappa})$ is a zero-mean, unit-variance complex-Gaussian (ZUCG) random field defined over $\mathcal{D}(\mathbf{k}) \times \mathcal{D}(\boldsymbol{\kappa})$, i.e., $W(\mathbf{k}, \boldsymbol{\kappa}) \sim \mathcal{CN}(0, 1)$ and its autocorrelation satisfies $\mathbb{E}\{W(\mathbf{k}, \boldsymbol{\kappa}) W^*(\mathbf{k}', \boldsymbol{\kappa}')\} = \delta(\mathbf{k} - \mathbf{k}') \delta(\boldsymbol{\kappa} - \boldsymbol{\kappa}')$, and $A_s(k_0) = \frac{2\pi}{k_0}$.

Substituting (4) into (23), we have

$$y_{c,\ell} = \sqrt{P} s_\ell \int_{\mathcal{A}_t} h_c(\mathbf{t}) w(\mathbf{t}) d\mathbf{t} + n_{c,\ell}. \quad (26)$$

Therefore, the CR is expressed as follows:

$$\mathcal{R}_c(w(\mathbf{t})) = \log_2 \left(1 + \bar{\gamma}_c \left| \int_{\mathcal{A}_t} h_c(\mathbf{t}) w(\mathbf{t}) d\mathbf{t} \right|^2 \right), \quad (27)$$

where $\bar{\gamma}_c \triangleq \frac{P}{\sigma_c^2}$.

By observing (27) and (22), we note that both communication and sensing performance in CAPA-based ISAC systems heavily depend on the source current pattern $w(\mathbf{t})$. Nevertheless, identifying an optimal $w(\mathbf{t})$ to simultaneously maximizes both the CR and SR is impossible. To tackle this issue and examine the fundamental performance limits of CAPA-based ISAC systems, we introduce three distinct continuous beamforming strategies: i) *the S-C design* that maximizes $\mathcal{R}_s(w(\mathbf{t}))$; ii) *the C-C design* that maximizes $\mathcal{R}_c(w(\mathbf{t}))$; iii) *the Pareto-optimal design* that identifies the Pareto boundary of the SR-CR region.

III. COMMUNICATION CHANNEL STATISTICS

In this section, we characterize the statistical properties for the communication channel.

By substituting (25) into (24), the communication channel response can be expressed as follows:

$$h_c(\mathbf{t}) = \frac{A_s(k_0)}{4\pi^2} \iint_{\mathcal{D}(\boldsymbol{\kappa})} \frac{e^{j\boldsymbol{\kappa}^T \mathbf{t}}}{\sqrt{\gamma(\boldsymbol{\kappa}_x, \boldsymbol{\kappa}_z)}} \hat{H}(\boldsymbol{\kappa}) d\boldsymbol{\kappa}, \quad (28)$$

where

$$\hat{H}(\boldsymbol{\kappa}) = \iint_{\mathcal{D}(\mathbf{k})} \frac{e^{-j\mathbf{k}^T \mathbf{p}_c}}{\sqrt{\gamma(k_x, k_z)}} W(\mathbf{k}, \boldsymbol{\kappa}) d\mathbf{k}. \quad (29)$$

Since $W(\mathbf{k}, \boldsymbol{\kappa})$ is a ZUCG random field, we can conclude that $\hat{H}(\boldsymbol{\kappa})$ is also a zero-mean complex-Gaussian random field. Given that $\mathbf{t} = [0, 0, z]^T$ for $z \in \mathcal{Z} \triangleq \{z \in \mathbb{R} | d/2 \leq z \leq d/2 + L_t\}$ and $\boldsymbol{\kappa} = [\boldsymbol{\kappa}_x, \gamma(\boldsymbol{\kappa}_x, \boldsymbol{\kappa}_z), \boldsymbol{\kappa}_z]^T$, (28) can be further simplified as follows:

$$h_c(\mathbf{t}) = \frac{A_s(k_0)}{4\pi^2} \int_{-k_0}^{k_0} e^{j\boldsymbol{\kappa}_z z} \hat{H}_z(\boldsymbol{\kappa}_z) d\boldsymbol{\kappa}_z \triangleq \hat{h}_c(z), \quad (30)$$

where

$$\hat{H}_z(\boldsymbol{\kappa}_z) = \int_{-\sqrt{k_0^2 - \boldsymbol{\kappa}_z^2}}^{\sqrt{k_0^2 - \boldsymbol{\kappa}_z^2}} \frac{\hat{H}(\boldsymbol{\kappa})}{\sqrt{\gamma(\boldsymbol{\kappa}_x, \boldsymbol{\kappa}_z)}} d\boldsymbol{\kappa}_x \quad (31)$$

is a zero-mean complex-Gaussian random field defined on $[-k_0, k_0]$. Therefore, the discussion above implies that the communication channel $\hat{h}_c(z)$ is a zero-mean complex-Gaussian random field defined on \mathcal{Z} , whose statistics are determined by its autocorrelation function given as follows.

Lemma 1. The autocorrelation function of $\hat{h}_c(z)$ is given by

$$R_c(z, z') = \frac{1}{2k_0} \int_{-k_0}^{k_0} e^{j\boldsymbol{\kappa}_z(z-z')} d\boldsymbol{\kappa}_z = \frac{\sin(k_0(z-z'))}{k_0(z-z')}. \quad (32)$$

Proof: Please refer to Appendix A for more details. ■

Given that $R_c(z, z')$ is a semi-positive definite Hilbert-Schmidt operator, we denote its eigendecomposition (EVD) of as follows:

$$R_c(z, z') = \sum_{n=1}^{\infty} \lambda_n \phi_n(z) \phi_n^*(z'), \quad (33)$$

where $\lambda_1 \geq \lambda_2 \geq \dots \geq \lambda_{\infty} \geq 0$ are the eigenvalues, and $\phi_n(z)$ is the associate eigenfunction satisfying

$$\int_{\mathcal{Z}} \phi_n(z) \phi_{n'}^*(z) dz = \delta_{n,n'} \quad (34)$$

for $n \in [1, 2, \dots, \infty]$ with $\delta_{n,n'}$ being the Kronecker delta. The eigenvalues can be evaluated numerically as outlined in

the Appendix B. On this basis, we can derive the following lemma.

Lemma 2. The statistics of the zero-mean complex-Gaussian random field $\hat{h}_c(z)$ satisfy

$$\hat{h}_c(z) \stackrel{d}{=} \sum_{n=1}^{\infty} \sqrt{\lambda_n} \phi_n(z) \Psi_n, \quad (35)$$

where $\stackrel{d}{=}$ represents equivalence in distribution, and $\{\Psi_n\}_{n=1}^{\infty}$ are independent and identically distributed (i.i.d.) ZUCG random variables.

Proof: Please refer to Appendix C for more details. ■

Based on Lemma 2, we can further deduce the statistics for the communication channel gain which is given by $g_c \triangleq \int_{\mathcal{A}_t} |h_c(\mathbf{t})|^2 dt = \int_{\mathcal{Z}} |\hat{h}_c(z)|^2 dz$ as follows.

Corollary 1. The statistics of the communication channel gain satisfy

$$g_c \stackrel{d}{=} \sum_{n=1}^{\infty} \lambda_n |\Psi_n|^2. \quad (36)$$

Since $\Psi_n \sim \mathcal{CN}(0, 1)$, we have $|\Psi_n|^2 \sim \text{Exp}(1)$. The results of (36) thus indicate that g_c is statistically equivalent to a weighted sum of an infinite number of i.i.d. exponentially distributed random variables.

Proof: Based on (35), we have

$$\begin{aligned} g_c &\stackrel{d}{=} \int_{\mathcal{Z}} \left| \sum_{n=1}^{\infty} \sqrt{\lambda_n} \phi_n(z) \Psi_n \right|^2 dz \\ &= \int_{\mathcal{Z}} \sum_{n=1}^{\infty} \sqrt{\lambda_n} \phi_n(z) \Psi_n \sum_{n'=1}^{\infty} \sqrt{\lambda_{n'}} \phi_{n'}^*(z) \Psi_{n'}^* dz \\ &= \sum_{n=1}^{\infty} \sum_{n'=1}^{\infty} \sqrt{\lambda_n \lambda_{n'}} \Psi_n \Psi_{n'}^* \int_{\mathcal{Z}} \phi_n(z) \phi_{n'}^*(z) dz \\ &= \sum_{n=1}^{\infty} \lambda_n |\Psi_n|^2. \end{aligned} \quad (37)$$

■

However, analyzing the statistics of an infinite weighted sum of exponentially distributed random variables is challenging. To address this, we explore more properties of the eigenvalues of $R_c(z, z')$, i.e., $\{\lambda_n\}_{n=1}^{\infty}$. In particular, we define

$$K(z, z') \triangleq \frac{1}{2\pi} \int_{-k_0}^{k_0} e^{j\boldsymbol{\kappa}_z(z-z')} d\boldsymbol{\kappa}_z = \frac{k_0}{\pi} R_c(z, z'), \quad z, z' \in \mathcal{Z}. \quad (38)$$

Let $\varepsilon_1 \geq \varepsilon_2 \geq \dots \geq \varepsilon_{\infty} \geq 0$ denote the eigenvalues of $K(z, z')$, which yields $\frac{\pi}{k_0} \varepsilon_n = \lambda_n$. For an arbitrary square-integrable function $f(z')$ defined on $z' \in \mathcal{Z}$, we introduce

$$\hat{f}(z) \triangleq \int_{\mathcal{Z}} K(z, z') f(z') dz', \quad z \in \mathcal{Z}, \quad (39)$$

which can be rewritten as follows:

$$\hat{f}(z) = \mathbf{1}_{\mathcal{Z}}(z) \int_{\mathcal{Z}} g(z-z') \mathbf{1}_{\mathcal{Z}}(z') f(z') dz'. \quad (40)$$

Here, $\mathbf{1}_{\mathcal{Z}}(\cdot)$ represent the indicator function over the set \mathcal{Z} , and the function $g(\cdot)$ is defined as

$$g(x) \triangleq \frac{1}{2\pi} \int_{-k_0}^{k_0} e^{jx\boldsymbol{\kappa}_z} d\boldsymbol{\kappa}_z, \quad x \in \mathbb{R}, \quad (41)$$

which corresponds to the inverse Fourier transform of $\mathbf{1}_{[-k_0, k_0]}(\boldsymbol{\kappa}_z)$. In other words, the Fourier transform of $g(x)$ is an ideal filter over the band $[-k_0, k_0]$. Consequently, according Landau's eigenvalue theorem [27], [28], the eigenvalues

$\{\varepsilon_n\}_{n=1}^{\infty}$ satisfy

$$1 \geq \varepsilon_1 \geq \varepsilon_2 \geq \dots \geq \varepsilon_{\infty} \geq 0, \quad (42)$$

and are governed by the effective DoFs:

$$\text{DoF} = \frac{1}{2\pi} \mu([-k_0, k_0]) \mu(\mathcal{Z}) = \frac{2k_0 L_t}{2\pi} = \frac{2L_t}{\lambda}. \quad (43)$$

As $L_t \rightarrow \infty$ or $\text{DoF} \rightarrow \infty$, the eigenvalues $\{\varepsilon_n\}_{n=1}^{\infty}$ asymptotically polarize. Specifically, for any $\varepsilon > 0$, it holds that

$$|n: \varepsilon_n > \varepsilon| = \text{DoF} + \left(\frac{1}{\pi^2} \log \frac{1 - \sqrt{\varepsilon}}{\sqrt{\varepsilon}} \right) \log \text{DoF} + o(\log \text{DoF}). \quad (44)$$

Remark 1. The results in (42) and (44) indicate that as L_t increases, the leading DoF eigenvalues $\{\varepsilon_n\}_{n=1}^{\text{DoF}}$ approach one, while the rest are near zero, with a transition band whose width scales proportionally to $\log \text{DoF}$.

These observations imply that, for small n , the eigenvalues λ_n decay slowly until reaching a critical point at $n = \text{DoF}$, beyond which they decrease rapidly. This step-like behavior becomes more pronounced as the physical length L_t increases. Since CAPAs are typically electromagnetically large arrays with $L_t \gg \lambda$, the sum $\sum_{n=1}^{\infty} \lambda_n |\Psi_n|^2$ is dominated by the first DoF terms, which yields

$$g_c \stackrel{d}{=} \sum_{n=1}^{\infty} \lambda_n |\Psi_n|^2 \approx \sum_{n=1}^{\text{DoF}} \lambda_n |\Psi_n|^2. \quad (45)$$

This suggests that the communication channel gain can be approximated as a finite weighted sum of i.i.d. exponentially distributed random variables, each following $\text{Exp}(1)$. Consequently, its PDF is given as follows.

Lemma 3. The PDF of communication channel gain $\int_{\mathcal{A}_t} |h_c(\mathbf{t})|^2 dt$ is given by [29]

$$f_g(x) = \frac{\lambda_{\text{DoF}}^{\text{DoF}}}{\prod_{n=1}^{\text{DoF}} \lambda_n} \sum_{m=0}^{\infty} \frac{\xi_m x^{\text{DoF}+m-1}}{\lambda_{\text{DoF}}^{\text{DoF}+m} \Gamma(\text{DoF}+m)} e^{-\frac{x}{\lambda_{\text{DoF}}}}, \quad (46)$$

where $\Gamma(x) = \int_0^{\infty} t^{x-1} e^{-t} dt$ is the Gamma function, $\xi_0 = 1$, and ξ_m ($m > 0$) is calculated recursively as $\xi_m = \frac{1}{m} \sum_{i=1}^m \xi_{m-i} \sum_{n=1}^{\text{DoF}} (1 - \lambda_{\text{DoF}}/\lambda_n)^i$.

IV. PERFORMANCE ANALYSIS

In this section, we analyze the performance of communications and sensing under the different beamforming designs.

A. Sensing-Centric Design

In the S-C design, the beamformer is designed to maximize the SR, which is given by

$$w_s(\mathbf{t}) = \underset{\int_{\mathcal{A}_t} |w(\mathbf{t})|^2 dt = 1}{\text{argmax}} \mathcal{R}_s(w(\mathbf{t})) = \frac{h_s^*(\mathbf{t})}{\sqrt{\int_{\mathcal{A}_t} |h_s(\mathbf{t})|^2 dt}}. \quad (47)$$

1) *Performance of Sensing:* Substituting $w(\mathbf{t}) = w_s(\mathbf{t})$ into (22) yields

$$\mathcal{R}_s^s = \frac{1}{L} \log_2 \left(1 + \bar{\gamma}_s L \alpha_s \int_{\mathcal{A}_r} |h_s(\mathbf{r})|^2 d\mathbf{r} \int_{\mathcal{A}_t} |h_s(\mathbf{t})|^2 dt \right). \quad (48)$$

A closed-form expression for \mathcal{R}_s^s is given as follows.

Theorem 1. In the S-C design, the SR can be expressed as follows:

$$\mathcal{R}_s^s = \frac{1}{L} \log_2 (1 + \bar{\gamma}_s L \alpha_s G_r G_t). \quad (49)$$

Here,

$$G_t = \frac{\zeta\left(\frac{d}{2}, \frac{d}{2} + L_t\right)}{4\pi \sqrt{p_{s,x}^2 + p_{s,y}^2}}, \quad G_r = \frac{\zeta\left(-\frac{d}{2} - L_r, -\frac{d}{2}\right)}{4\pi \sqrt{p_{s,x}^2 + p_{s,y}^2}}, \quad (50)$$

where $\zeta(x, y) \triangleq \arctan\left(\frac{y - p_{s,z}}{\sqrt{p_{s,x}^2 + p_{s,y}^2}}\right) - \arctan\left(\frac{x - p_{s,z}}{\sqrt{p_{s,x}^2 + p_{s,y}^2}}\right)$.

Proof: Please refer to Appendix D for more details. ■

To gain further insights, we then examine the asymptotic SR in the high-SNR regime to obtain the maximal multiplexing gain, i.e., the high-SNR slope, which is defined as

$$S_i = \lim_{P \rightarrow \infty} \frac{\mathcal{R}_i}{\log_2 P}, \quad i \in \{c, s\}. \quad (51)$$

Corollary 2. As $P \rightarrow \infty$, the asymptotic SR of the S-C design satisfies

$$\mathcal{R}_s^s \simeq \frac{1}{L} \log_2 \bar{\gamma}_s + \frac{1}{L} \log_2 (L \alpha_s G_r G_t). \quad (52)$$

This suggests that the high-SNR slope of the SR achieved by the S-C design is $\frac{1}{L}$.

Proof: The results can be easily obtained based on the fact $\lim_{x \rightarrow \infty} \log_2(1+x) \simeq \log_2 x$. ■

2) *Performance of Communications:* By inserting $w(\mathbf{t}) = w_s(\mathbf{t})$ into (27), the CR under the S-C design is expressed as

$$\mathcal{R}_c^s = \log_2 \left(1 + \bar{\gamma}_c \frac{|\rho|^2}{\int_{\mathcal{A}_t} |h_s(\mathbf{t})|^2 dt} \right), \quad (53)$$

where $\rho \triangleq \int_{\mathcal{A}_t} h_c(\mathbf{t}) h_s^*(\mathbf{t}) dt$ is a random variable. In the following theorem, we derive the ECR.

Theorem 2. In the S-C design, the ECR, i.e., $\bar{\mathcal{R}}_c^s = \mathbb{E}\{\mathcal{R}_c^s\}$, can be expressed as follows:

$$\bar{\mathcal{R}}_c^s = -\frac{1}{\ln 2} e^{\frac{G_t}{\bar{\gamma}_c \Xi}} \text{Ei}\left(-\frac{G_t}{\bar{\gamma}_c \Xi}\right), \quad (54)$$

where $\Xi = \int_{\mathcal{Z}} \int_{\mathcal{Z}'} \hat{h}_s(z) R_c(z, z') \hat{h}_s^*(z') dz dz'$ with $\hat{h}_s(z)$ defined as (A12), and $\text{Ei}(x) = -\int_{-x}^{\infty} \frac{e^{-t}}{t} dt$ is the exponential integral function.

Proof: Please refer to Appendix E for more details. ■

Corollary 3. The high-SNR ECR under the S-C design satisfies

$$\bar{\mathcal{R}}_c^s \simeq \log_2 \bar{\gamma}_c - \log_2 \frac{G_t}{\Xi} - \frac{\mathcal{C}}{\ln 2}, \quad (55)$$

where $\mathcal{C} \approx 0.5772$ is the Euler constant. This suggests that the high-SNR slope of the CR achieved by the S-C design is one.

Proof: When $P \rightarrow \infty$, the CR can be approximated as $\mathcal{R}_c^s \simeq \log_2 \left(\bar{\gamma}_c \frac{\int_{\mathcal{A}_t} h_c(\mathbf{t}) h_s^*(\mathbf{t}) dt}{\int_{\mathcal{A}_t} |h_s(\mathbf{t})|^2 dt} \right)$, and thus the ECR can be calculated based on Appendix E and [30, (4.331.1)]. ■

Next, we analyze the OP, which is defined as

$$\mathcal{P} = \Pr(\mathcal{R}_c < \mathcal{R}_0), \quad (56)$$

where \mathcal{R}_0 denotes the target rate.

Theorem 3. The communication OP in the S-C design can be expressed in closed form as follows:

$$\mathcal{P}_s = 1 - e^{-\frac{G_t}{\bar{\gamma}_c \Xi} (2^{\mathcal{R}_0} - 1)}. \quad (57)$$

Proof: Please refer to Appendix E for more details. ■

We then consider the high-SNR OP to obtain the maximal diversity gain, i.e., the diversity order, which is defined as

$$\mathcal{D} = - \lim_{P \rightarrow \infty} \frac{\log_2 P}{\log_2 P}. \quad (58)$$

Corollary 4. As $P \rightarrow \infty$, the asymptotic OP of the S-C design satisfies

$$\mathcal{P}_s \simeq \frac{G_t}{\bar{\gamma}_c \Xi} (2^{\mathcal{R}_0} - 1). \quad (59)$$

This suggests that the diversity order achieved by the C-C design is one.

Proof: (59) is obtained by applying the fact $\lim_{x \rightarrow 0} e^{-x} \simeq 1 - x$ to (57). ■

B. Communications-Centric Design

In the C-C design, the continuous beamformer is designed to maximize the CR, given by

$$w_c(\mathbf{t}) = \underset{\int_{\mathcal{A}_t} |w(\mathbf{t})|^2 dt = 1}{\operatorname{argmax}} \mathcal{R}_c(w(\mathbf{t})) = \frac{h_c^*(\mathbf{t})}{\sqrt{\int_{\mathcal{A}_t} |h_c(\mathbf{t})|^2 dt}}. \quad (60)$$

1) *Performance of Communications:* Substituting $w(\mathbf{t}) = w_c(\mathbf{t})$ into (27), the CR is expressed as follows:

$$\mathcal{R}_c^c = \log_2(1 + \bar{\gamma}_c g_c). \quad (61)$$

Based on **Lemma 3**, the following theorem can be found.

Theorem 4. In the C-C design, the ECR $\mathbb{E}\{\mathcal{R}_c^c\}$ is given by

$$\begin{aligned} \bar{\mathcal{R}}_c^c &= \frac{\lambda_{\text{DoF}}^{\text{DoF}}}{\ln 2 \prod_{n=1}^{\text{DoF}} \lambda_n} \sum_{m=0}^{\text{DoF}+m-1} \sum_{u=0}^{\text{DoF}+m-1} \frac{\xi_m}{(\text{DoF} + m - u - 1)!} \\ &\times \left[\frac{(-1)^{\text{DoF}+m-u} e^{1/(\bar{\gamma}_c \lambda_{\text{DoF}})}}{(\bar{\gamma}_c \lambda_{\text{DoF}})^{\text{DoF}+m-u-1}} \operatorname{Ei} \left(-\frac{1}{\bar{\gamma}_c \lambda_{\text{DoF}}} \right) \right. \\ &\left. + \sum_{l=1}^{\text{DoF}+m-u-1} (l-1)! \left(-\frac{1}{\bar{\gamma}_c \lambda_{\text{DoF}}} \right)^{\text{DoF}+m-u-1-l} \right]. \end{aligned} \quad (62)$$

Proof: The ECR is calculated as

$$\begin{aligned} \bar{\mathcal{R}}_c^c &= \mathbb{E} \{ \log_2(1 + \bar{\gamma}_c g_c) \} \\ &= \frac{1}{\ln 2} \int_0^\infty \ln(1 + \bar{\gamma}_c x) f_g(x) dx. \end{aligned} \quad (63)$$

By substituting (46) into (63) and using [30, (4.337.5)], the results of (62) can be obtained. ■

Corollary 5. The asymptotic ECR achieved by the C-C design in the high-SNR regime is given by

$$\bar{\mathcal{R}}_c^c \simeq \log_2 \bar{\gamma}_c + \frac{\lambda_{\text{DoF}}^{\text{DoF}} \log_2 e}{\prod_{n=1}^{\text{DoF}} \lambda_n} \sum_{m=0}^{\infty} \xi_m (\psi(\text{DoF} + m) + \ln(\lambda_{\text{DoF}})), \quad (64)$$

where $\psi(x) = \frac{d}{dx} \ln \Gamma(x)$ is the digamma function. This suggests that the high-SNR slope of the CR achieved by the C-C design is one.

Proof: When $P \rightarrow \infty$, the CR can be approximated as $\mathcal{R}_c^c \simeq \log_2(\bar{\gamma}_c g_c)$, and thus the ECR is given by

$$\bar{\mathcal{R}}_c^c \simeq \log_2 \bar{\gamma}_c + \int_0^\infty \log_2 x f_g(x) dx, \quad (65)$$

which can be calculated by using [30, (4.352.1)]. ■

We then study the OP. The following theorem provides a closed-form expression of the OP.

Theorem 5. The OP of the C-C design can be expressed as

$$\mathcal{P}_c = \frac{\lambda_{\text{DoF}}^{\text{DoF}}}{\prod_{n=1}^{\text{DoF}} \lambda_n} \sum_{m=0}^{\infty} \frac{\xi_m \gamma(\text{DoF} + m, \frac{2^{\mathcal{R}_0} - 1}{\bar{\gamma}_c \lambda_{\text{DoF}}})}{(\text{DoF} + m - 1)!}, \quad (66)$$

where $\gamma(s, x) = \int_0^x t^{s-1} e^{-t} dt$ represents the lower incomplete gamma function.

Proof: By performing some manipulations, the OP can be written as $\mathcal{P}_c = F_g \left(\frac{2^{\mathcal{R}_0} - 1}{\bar{\gamma}_c} \right)$, where $F_g(\cdot)$ denotes the CDF of g_c . With the aid of [30, (3.351.1)], $F_g(x)$ can be calculated as follows:

$$F_g(x) = \int_0^x f_g(t) dt = \frac{\lambda_{\text{DoF}}^{\text{DoF}}}{\prod_{n=1}^{\text{DoF}} \lambda_n} \sum_{m=0}^{\infty} \frac{\xi_m \gamma(\text{DoF} + m, \frac{x}{\lambda_{\text{DoF}}})}{(\text{DoF} + m - 1)!}, \quad (67)$$

which yields the results of (66). ■

Corollary 6. As $P \rightarrow \infty$, the asymptotic OP of the C-C design satisfies

$$\mathcal{P}_c \simeq \frac{(2^{\mathcal{R}_0} - 1)^{\text{DoF}}}{\bar{\gamma}_c^{\text{DoF}} \text{DoF}! \prod_{n=1}^{\text{DoF}} \lambda_n}. \quad (68)$$

This suggests that the diversity order achieved by the C-C design is DoF.

Proof: The results of (68) is obtained by applying the fact $\lim_{x \rightarrow 0} \gamma(s, x) \simeq \frac{x^s}{s}$ based on [30, (8.354.1)] to (66). ■

2) *Performance of Sensing:* When the C-C beamformer $w_c(\mathbf{t})$ is employed, the SR is given by

$$\mathcal{R}_s^c = \frac{1}{L} \log_2 \left(1 + L \alpha_s \bar{\gamma}_s \int_{\mathcal{A}_t} |h_s(\mathbf{r})|^2 d\mathbf{r} \frac{\left| \int_{\mathcal{A}_t} h_s(\mathbf{t}) h_c^*(\mathbf{t}) dt \right|^2}{\int_{\mathcal{A}_t} |h_c(\mathbf{t})|^2 dt} \right), \quad (69)$$

which can be further rewritten as follows.

Lemma 4. The SR under the C-C design can be written as

$$\mathcal{R}_s^c = \frac{1}{L} \log_2 \left(\sum_{n=1}^{\text{DoF}_Q} \nu_n |\Phi_n|^2 \right) - \frac{1}{L} \log_2 g_c, \quad (70)$$

where $\{\nu_n\}_{n=1}^{\infty}$ are the eigenvalues of $Q(z_1, z_2) \triangleq \int_{\mathcal{Z}} \int_{\mathcal{Z}} \tilde{R}_c(z_1, z) (\delta(z - z') + L \alpha_s \bar{\gamma}_s G_t \hat{h}_s(z) \hat{h}_s^*(z')) \tilde{R}_c(z', z_2) dz dz'$ with $\tilde{R}_c(z, z_1) = \sum_{n=1}^{\text{DoF}} \sqrt{\lambda_n} \phi_n(z) \phi_n^*(z_1)$, DoF_Q denotes the DoF of $Q(z_1, z_2)$, and $\{\Phi_n\}_{n=1}^{\infty}$ are i.i.d. ZUCG random variables. Note that $\{\nu_n\}_{n=1}^{\infty}$ can be obtained using a method similar to that described in Appendix B.

Proof: Please refer to Appendix F for more details. ■

Based on Lemma 4, a closed-form expression for the average SR defined as $\bar{\mathcal{R}}_s^c = \mathbb{E}\{\mathcal{R}_s^c\}$ is derived as follows.

Theorem 6. In the C-C design, the average SR is given by

$$\begin{aligned} \bar{\mathcal{R}}_s^c &= \frac{\nu_{\text{DoF}_Q}^{\text{DoF}_Q} \log_2 e}{L \prod_{n=1}^{\text{DoF}_Q} \nu_n} \sum_{m=0}^{\infty} \xi_m (\psi(\text{DoF}_Q + m) + \ln(\nu_{\text{DoF}_Q})) \\ &\quad - \frac{\lambda_{\text{DoF}}^{\text{DoF}} \log_2 e}{L \prod_{n=1}^{\text{DoF}} \lambda_n} \sum_{m=0}^{\infty} \xi_m (\psi(\text{DoF} + m) + \ln(\lambda_{\text{DoF}})). \end{aligned} \quad (71)$$

Proof: The results are obtained by using [30, (4.352.1)]. ■

Corollary 7. The high-SNR average SR under the C-C design satisfies

$$\begin{aligned} \bar{\mathcal{R}}_s^c &\simeq \frac{1}{L} \left(\log_2 \bar{\gamma}_c + \log_2(L\alpha_s G_r \Xi) - \frac{C}{\ln 2} \right) \\ &\quad - \frac{\lambda_{\text{DoF}}^{\text{DoF}} \log_2 e}{L \prod_{n=1}^{\text{DoF}} \lambda_n} \sum_{m=0}^{\infty} \xi_m (\psi(\text{DoF} + m) + \ln(\lambda_{\text{DoF}})). \end{aligned} \quad (72)$$

This suggests that the high-SNR slope of the CR achieved by the C-C design is $\frac{1}{L}$.

Proof: When $P \rightarrow \infty$, (69) can be rewritten as follows:

$$\mathcal{R}_s^c \simeq \frac{1}{L} \log_2 \left(L\alpha_s \bar{\gamma}_s G_r |\rho|^2 \right) - \frac{1}{L} \log_2 g_c. \quad (73)$$

The average SR can be then calculated by following the steps similar to the proofs of Corollary 3 and 5. ■

By comparing the sensing and communication performance of the S-C and C-C designs, we have the following observations.

Remark 2. The S-C and C-C designs achieve the same multiplexing gains for both sensing and communications, whereas the C-C design provides a higher diversity gain than the S-C design.

C. Pareto-Optimal Design

In real-world implementations, the beamformer $w(\mathbf{t})$ can be tailored to satisfy different quality-of-service demands, inevitably leading to a balance between communication and sensing performance. To assess this balance, we analyze the Pareto boundary of the achievable SR–CR region in the CAPA-based ISAC framework. This boundary consists of SR–CR pairs where enhancing one rate necessarily results in the degradation of the other. It effectively depicts the optimal trade-off between sensing and communication functionalities and offers key insights for system optimization.

It should be emphasized that the SR monotonically increases with respect to $|\int_{\mathcal{A}_t} h_s(\mathbf{t})w(\mathbf{t})d\mathbf{t}|^2 \triangleq \Upsilon_s(w(\mathbf{t}))$, while the CR exhibits a similar monotonic relationship with $|\int_{\mathcal{A}_t} h_c(\mathbf{t})w(\mathbf{t})d\mathbf{t}|^2 \triangleq \Upsilon_c(w(\mathbf{t}))$. Consequently, the achievable SR–CR region can be characterized through the $\hat{\gamma}_c(w(\mathbf{t}))$ - $\hat{\gamma}_s(w(\mathbf{t}))$ space. Specifically, any point lying on the Pareto boundary of this region can be determined by solving the following optimization problem:

$$\max_{w(\mathbf{t}), \Upsilon} \Upsilon \quad (74a)$$

$$\text{s.t. } \Upsilon_s(w(\mathbf{t})) \geq \tau \Upsilon, \quad \Upsilon_c(w(\mathbf{t})) \geq (1 - \tau) \Upsilon, \quad (74b)$$

$$\int_{\mathcal{A}_t} |w(\mathbf{t})|^2 d\mathbf{t} = 1, \quad (74c)$$

where $\tau \in [0, 1]$ is a trade-off parameter. The entire Pareto boundary is determined by solving the above problem with

τ varying from 0 to 1, which belongs to the class of non-convex integral-based functional programming. To solve such a challenging problem, we introduce a *subspace approach* as follows.

Lemma 5. For a given τ , the Pareto-optimal beamformer lies in the subspace spanned by $\{h_s^*(\mathbf{t}), h_c^*(\mathbf{t})\}$, i.e., $w(\mathbf{t}) = ah_c^*(\mathbf{t}) + bh_s^*(\mathbf{t})$, where $a, b \in \mathbb{C}$.

Proof: Please refer to Appendix G for more details. ■

Based on Lemma 5, we denote $\{\phi_1(\mathbf{t}), \phi_2(\mathbf{t})\}$ as an orthonormal basis for the signal subspace spanned by $\{h_s^*(\mathbf{t}), h_c^*(\mathbf{t})\}$, which satisfies

$$\int_{\mathcal{A}_t} \phi_i^*(\mathbf{t})\phi_j(\mathbf{t})d\mathbf{t} = \delta_{i,j}, \quad \forall i, j \in \{1, 2\}, \quad (75)$$

where $\delta_{i,j}$ denotes the Kronecker delta. The beamformer and channels can be expressed in terms of the basis as follows:

$$w(\mathbf{t}) = w_1\phi_1(\mathbf{t}) + w_2\phi_2(\mathbf{t}), \quad (76a)$$

$$h_s^*(\mathbf{t}) = h_{s,1}\phi_1(\mathbf{t}) + h_{s,2}\phi_2(\mathbf{t}), \quad (76b)$$

$$h_c^*(\mathbf{t}) = h_{c,1}\phi_1(\mathbf{t}) + h_{c,2}\phi_2(\mathbf{t}). \quad (76c)$$

Defining the vector representations: $\mathbf{w} = [w_1, w_2]^T$, $\mathbf{h}_s = [h_{s,1}, h_{s,2}]^T$, and $\mathbf{h}_c = [h_{c,1}, h_{c,2}]^T$, we have $\|\mathbf{h}_s\|^2 = \int_{\mathcal{A}_t} |h_s(\mathbf{t})|^2 d\mathbf{t} = G_t$, $\|\mathbf{h}_c\|^2 = \int_{\mathcal{A}_t} |h_c(\mathbf{t})|^2 d\mathbf{t} = g_c$, and $\mathbf{h}_s^H \mathbf{h}_c = \int_{\mathcal{A}_t} h_c(\mathbf{t})h_s^*(\mathbf{t})d\mathbf{t} = \rho$. Furthermore, the integrals can be transformed into the following forms:

$$\int_{\mathcal{A}_t} h_s(\mathbf{t})w(\mathbf{t})d\mathbf{t} = \mathbf{h}_s^T \mathbf{w}, \quad \int_{\mathcal{A}_t} h_c(\mathbf{t})w(\mathbf{t})d\mathbf{t} = \mathbf{h}_c^T \mathbf{w}, \quad (77a)$$

$$\int_{\mathcal{A}_t} |w(\mathbf{t})|^2 d\mathbf{t} = \|\mathbf{w}\|^2 = 1, \quad (77b)$$

Consequently, problem (74) can be equivalently rewritten as follows:

$$\max_{\mathbf{w}, \Upsilon} \Upsilon \quad \text{s.t. } |\mathbf{h}_s^T \mathbf{w}|^2 \geq \tau \Upsilon, \quad |\mathbf{h}_c^T \mathbf{w}|^2 \geq (1 - \tau) \Upsilon, \quad \|\mathbf{w}\|^2 = 1. \quad (78)$$

By employing the subspace approach, the originally intractable functional programming problem is converted to problem (78), which is a classical vector-based optimization problem that can be solved using the Karush–Kuhn–Tucker (KKT) conditions.

Lemma 6. For a given τ , the Pareto-optimal solution for problem (78) is given by

$$\mathbf{w}_\tau = \begin{cases} \frac{\mathbf{h}_c^*}{\sqrt{g_c}} & \tau \in \left[0, \frac{|\rho|^2}{|\rho|^2 + g_c^2}\right] \\ \frac{\epsilon_1}{\varsigma} \mathbf{h}_s^* + \frac{\epsilon_2 e^{-j\angle \rho}}{\varsigma} \mathbf{h}_c^* & \tau \in \left(\frac{|\rho|^2}{|\rho|^2 + g_c^2}, \frac{G_t^2}{G_t^2 + |\rho|^2}\right) \\ \frac{\mathbf{h}_s^*}{\sqrt{G_t}} & \tau \in \left[\frac{G_t^2}{G_t^2 + |\rho|^2}, 1\right] \end{cases}, \quad (79)$$

where $\epsilon_1 = \frac{\sqrt{\tau}g_c - \sqrt{(1-\tau)}|\rho|}{(1-\tau)G_t + \tau g_c - 2\sqrt{\tau(1-\tau)}|\rho|}$, $\epsilon_2 = \frac{\sqrt{(1-\tau)}G_t - \sqrt{\tau}|\rho|}{(1-\tau)G_t + \tau g_c - 2\sqrt{\tau(1-\tau)}|\rho|}$, and $\varsigma = \sqrt{\epsilon_1^2 G_t + \epsilon_2^2 g_c + 2\epsilon_1 \epsilon_2 |\rho|}$ is for normalization.

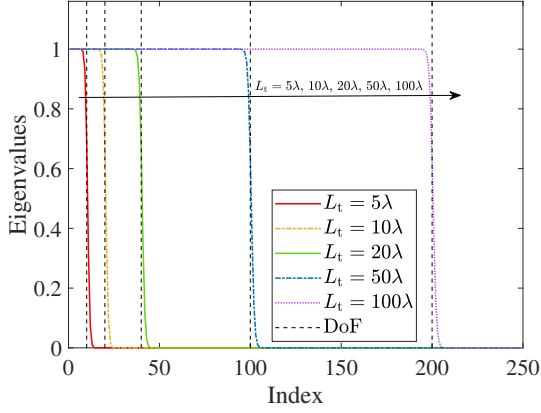
Proof: Please refer to Appendix H for more details. ■

Having obtain \mathbf{w}_τ , based on (76), we can derive the Pareto-optimal continuous beamformer for problem (74).

Theorem 7. For a given τ , the Pareto-optimal continuous

TABLE I: High-SNR Slopes (\mathcal{S}) and Diversity Orders (\mathcal{D})

System design	SR	ECR	
	\mathcal{S}	\mathcal{S}	\mathcal{D}
CAPA-ISAC S-C	$1/L$	1	1
CAPA-ISAC C-C	$1/L$	1	DoF
CAPA-ISAC Pareto-optimal	$1/L$	1	$[1, \text{DoF}]$
SPDA ($d_s \leq \lambda/2$) S-C	$1/L$	1	1
SPDA ($d_s \leq \lambda/2$) C-C	$1/L$	1	DoF
SPDA ($d_s > \lambda/2$) S-C	$1/L$	1	1
SPDA ($d_s > \lambda/2$) C-C	$1/L$	1	L_t/d_s
FDSAC	κ/L	$1 - \kappa$	DoF

Fig. 2: Illustration of the eigenvalues of $K(z, z')$.

beamformer is given by

$$w_\tau(\mathbf{t}) = \begin{cases} w_c(\mathbf{t}) & \tau \in \left[0, \frac{|\rho|^2}{|\rho|^2 + g_c^2}\right] \\ \frac{\epsilon_1}{\varsigma} h_s^*(\mathbf{t}) + \frac{\epsilon_2 e^{-j\angle \rho}}{\varsigma} h_c^*(\mathbf{t}) & \tau \in \left(\frac{|\rho|^2}{|\rho|^2 + g_c^2}, \frac{G_t^2}{G_t^2 + |\rho|^2}\right) \\ w_s(\mathbf{t}) & \tau \in \left[\frac{G_t^2}{G_t^2 + |\rho|^2}, 1\right] \end{cases}. \quad (80)$$

Remark 3. The results of Theorem 7 suggest that the Pareto-optimal beamformer is a weighted combination of $\{h_s^*(\mathbf{t}), h_c^*(\mathbf{t})\}$. In particular, it reduces to the S-C beamformer when $\tau \in \left[\frac{G_t^2}{G_t^2 + |\rho|^2}, 1\right]$, and to the C-C beamformer when $\tau \in \left[0, \frac{|\rho|^2}{|\rho|^2 + g_c^2}\right]$.

For a given τ , let $(\mathcal{R}_s^\tau, \overline{\mathcal{R}_c}^\tau)$ represent the SR-CR pair located on the Pareto boundary. Therefore, we have $\mathcal{R}_s^\tau \in [\mathcal{R}_s^c, \mathcal{R}_s^s]$ and $\overline{\mathcal{R}_c}^\tau \in [\overline{\mathcal{R}_c}^s, \overline{\mathcal{R}_c}^c]$, where $\mathcal{R}_s^0 = \mathcal{R}_s^c$, $\mathcal{R}_s^1 = \mathcal{R}_s^s$, $\overline{\mathcal{R}_c}^0 = \overline{\mathcal{R}_c}^c$, and $\overline{\mathcal{R}_c}^1 = \overline{\mathcal{R}_c}^s$. Based on the Sandwich theorem, we can obtain the high-SNR slopes and diversity orders for any SR-CR pair on the Pareto boundary, as outlined in Table I. Consequently, the achievable SR-CR region of the CAPA-based ISAC system can be characterized as follows:

$$\mathcal{C} = \left\{ (\mathcal{R}_s, \mathcal{R}_c) \mid \mathcal{R}_s \in [0, \mathcal{R}_s^\tau], \mathcal{R}_c \in [0, \overline{\mathcal{R}_c}^\tau], \tau \in [0, 1] \right\}. \quad (81)$$

V. NUMERICAL RESULTS

In this section, we present numerical results to evaluate the performance of CAPA-based ISAC systems and to validate the accuracy of the derived analytical expressions. Unless other-

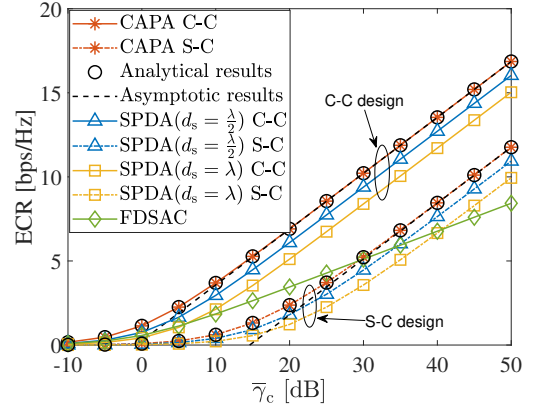


Fig. 3: ECR versus transmit SNR.

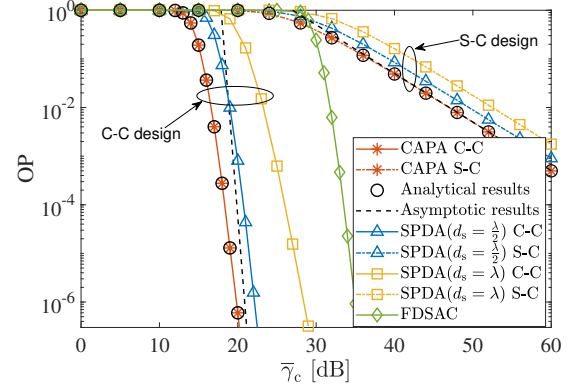


Fig. 4: OP versus transmit SNR.

wise specified, the simulation parameters are set as follows: the wavelength is given by $\lambda = 0.125$ m, $L_t = L_r = 10\lambda$, $d = 2\lambda$, $\overline{\gamma}_s = \overline{\gamma}_c = 50$ dB, $L = 4$, $\alpha_s = 1$, and $R_0 = 5$ bps/Hz. The target and CU are located at $\mathbf{p}_s = [2 \text{ m}, 1 \text{ m}, 1 \text{ m}]$ and $\mathbf{p}_c = [4 \text{ m}, 0 \text{ m}, 0 \text{ m}]$, respectively.

In Fig. 2, we illustrates the ordered eigenvalues of $K(z, z')$ for different array lengths L_t , computed using the method in Appendix B. The complexity-vs-accuracy trade-off parameter is set to $T = 1000$. It can be observed from the figure that the eigenvalues of $K(z, z')$ exhibit a step-like behavior: for indexes below the effective DoF, i.e., $\frac{2L_t}{\lambda}$, the eigenvalues decay slowly and are nearly one; in contrast, when the index is larger than the DoF, the eigenvalues drop rapidly towards zero. This behavior is consistent with the statements in Remark 1. Notably, this step-like behavior is already pronounced for moderate array sizes, e.g., $L_t = 10\lambda$. This observation underpins our earlier analysis of the communication channel gain, which models it as a finite weighted sum of exponentially distributed random variables.

In the following results, we consider two baseline schemes for comparison:

- **SPDA-based ISAC:** Both the transmit and receive arrays are SPDAs, where each element has length $\sqrt{\frac{\lambda^2}{4\pi}}$. The inter-element spacing is denoted by d_s .
- **CAPA-based FDSAC:** For FDSAC, a fraction $\kappa = 0.5$ of the total bandwidth and a fraction $\iota = 0.5$ of the transmit power are allocated exclusively to sensing, while the remaining fractions are used

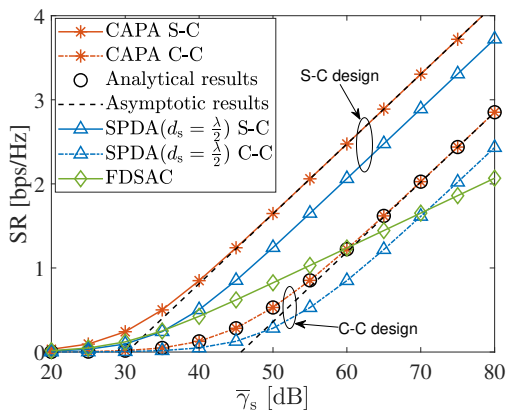


Fig. 5: SR versus transmit SNR.

for communications. In this case, the SR and ECR are given by $\mathcal{R}_s^f = \frac{\kappa}{L} \log_2 \left(1 + \frac{\kappa}{L} \bar{\gamma}_s L \alpha_s G_r G_t \right)$ and $\bar{\mathcal{R}}_c^f = \mathbb{E} \left\{ (1 - \kappa) \log_2 \left(1 + \frac{1 - \kappa}{1 - \kappa} \bar{\gamma}_c g_c \right) \right\}$, respectively. Moreover, the achievable SR-CR region of FDSAC is characterized as

$$\mathcal{C}_f = \left\{ (\mathcal{R}_s, \mathcal{R}_c) \left| \begin{array}{l} \mathcal{R}_s \in [0, \mathcal{R}_s^f], \mathcal{R}_c \in [0, \bar{\mathcal{R}}_c^f], \\ \kappa \in [0, 1], \nu \in [0, 1] \end{array} \right. \right\}. \quad (82)$$

Fig. 3 and 4 plot the ECR and OP versus the communication transmit SNR $\bar{\gamma}_c$, respectively. It can be seen that the derived analytical results match well with the Monte Carlo simulation results, and the asymptotic results accurately track the simulation results in the high-SNR regime. As expected, the C-C design for CAPA-ISAC achieves the best communication performance. For the ECR, the C-C and S-C designs exhibit the same high-SNR slope, which is higher than that of FDSAC. On the other hand, for outage performance, the diversity orders achieved by the C-C design is significantly higher than that of the S-C design. These observations corroborate the conclusion in Remark 2.

Additionally, we can observe that CAPA consistently outperforms the conventional SPDA. In particular, CAPA attains a diversity order comparable to that of SPDA with $d_s = \frac{\lambda}{2}$, while outperforming SPDA with $d_s = \lambda$. This can be explained by the effective spatial DoFs. When the SPDA elements are spaced at sub-half-wavelength intervals, the number of the elements is no smaller than $\frac{2L_t}{\lambda} = \text{DoF}$, and the rank of the channel correlation channel matrix reaches DoF. Consequently, SPDA is able to maintain the same DoFs and diversity gain as CAPA. However, when the spacing exceeds half a wavelength, the number of SPDA elements (and hence the rank of the correlation matrix) falls below DoF, resulting in reduced DoF and diversity gain compared with CAPA. For ease of comparison, the high-SNR slopes and diversity orders achieved by each design and baseline scheme are summarised in Table I.

Fig. 5 plots the SR versus the sensing SNR $\bar{\gamma}_s$, validating the accuracy of both the analytical and asymptotic results. As can be seen, CAPA-based S-C ISAC achieves the best sensing performance. Importantly, CAPA attains a higher SR than SPDA, while both schemes exhibit the same high-SNR slope. Additionally, in the high-SNR regime, the SR curves of

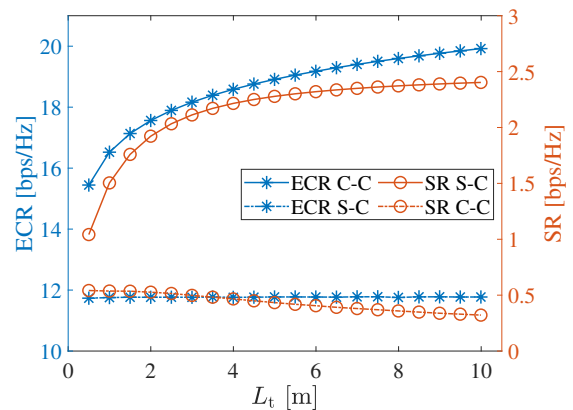


Fig. 6: Rates versus transmit aperture length.

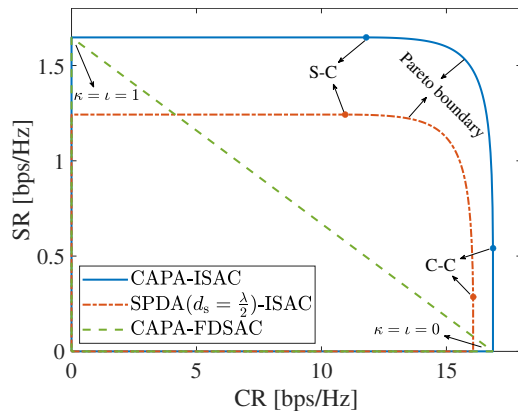


Fig. 7: Achievable SR-CR regions.

ISAC increase more steeply than that of FDSAC, indicating that ISAC provides a larger sensing DoFs than conventional FDSAC.

Fig. 6 plots the ECR and SR achieved by CAPA as functions of L_t . It is worth to note that the ECR under the S-C design exhibits weak sensitivity to the aperture length. This is because the closed-form results in (54) shows that ECR depends on L_t primarily through the ratio $\frac{G_t}{\Xi}$, which is the variance of $\rho \triangleq \int_{\mathcal{A}_t} h_c(t) h_s^*(t) dt$. Enlarging L_t scales both G_t and Ξ in a similar order, so $\frac{G_t}{\Xi}$ remains approximately constant, leading to only marginal changes in ECR with L_t . This is also reflected in the high-SNR approximation in (55), where the ECR is dominated by $-\log_2 \frac{G_t}{\Xi}$. Moreover, increasing the transmit aperture length can even decrease the SR under the C-C design. From (69), the SR depends on the ratio $\frac{|\rho|^2}{g_c}$. When L_t grows, the C-C beamformer becomes increasingly concentrated on maximizing the communication link, which typically boosts g_c more rapidly than $|\rho|^2$, thereby decreasing the SR. Overall, these results indicate that aperture enlargement yields clear benefits only when the beamformer remains aligned with the target metric, which motivates the proposed Pareto trade-off design that balances the S-C and C-C beamformers.

Fig. 7 shows the achievable SR-CR regions achieved by three schemes: CAPA-based ISAC (defined in (81)), SPDA-based ISAC, and CAPA-based FDSAC (defined in (82)). For the ISAC scheme, two corner points are highlighted,

corresponding to the S-C and C-C designs. By continuously adjusting the trade-off parameter τ from 1 to 0, we obtain a curve connecting these points, which forms the Pareto boundary of the ISAC rate region. A key observation is that the regions attainable by both SPDA-ISAC and CAPA-FDSAC lie strictly inside the CAPA-ISAC region, demonstrating the advantage of the proposed CAPA-based ISAC framework in jointly improving and balancing sensing and communication performance.

VI. CONCLUSION

This article developed an operator-based framework for CAPA-enabled ISAC under a fading communication channel. By modeling the communication link as a continuous random field and leveraging the spectral structure of its correlation operator (via Landau's eigenvalue theorem), we obtained a tractable characterization of the channel-gain statistics and, in turn, derived closed-form expressions for key metrics including SRs, ECRs, and OPs under the S-C and C-C designs, together with interpretable high-SNR asymptotics that reveal multiplexing and diversity behaviors. We further characterized the Pareto boundary of the achievable SR-CR region. Numerical results validate the analysis and demonstrate that the achievable SR-CR region of CAPA-based ISAC strictly contains those of both SPDA-based ISAC and CAPA-based FDSAC, confirming CAPA's advantage in jointly improving and balancing sensing and communication performance.

APPENDIX

A. Proof of Lemma 1

We first calculate the autocorrelation of $\hat{H}(\boldsymbol{\kappa})$. We define $\frac{e^{-j\mathbf{k}^T \mathbf{p}_c}}{\sqrt{\gamma(\kappa_x, \kappa_z)}} \triangleq \zeta(\mathbf{k})$, which yields

$$\begin{aligned} & \mathbb{E} \left\{ \hat{H}(\boldsymbol{\kappa}) \hat{H}^*(\boldsymbol{\kappa}') \right\} \\ &= \mathbb{E} \left\{ \iint_{\mathcal{D}(\mathbf{k})} \zeta(\mathbf{k}) W(\mathbf{k}, \boldsymbol{\kappa}) d\mathbf{k} \iint_{\mathcal{D}(\mathbf{k}')} \zeta^*(\mathbf{k}') W^*(\mathbf{k}', \boldsymbol{\kappa}') d\mathbf{k}' \right\} \\ &= \iint_{\mathcal{D}(\mathbf{k})} \iint_{\mathcal{D}(\mathbf{k}')} \zeta(\mathbf{k}) \zeta^*(\mathbf{k}') \mathbb{E} \{ W(\mathbf{k}, \boldsymbol{\kappa}) W^*(\mathbf{k}', \boldsymbol{\kappa}') \} d\mathbf{k}' d\mathbf{k} \\ &= \iint_{\mathcal{D}(\mathbf{k})} \iint_{\mathcal{D}(\mathbf{k}')} \zeta(\mathbf{k}) \zeta^*(\mathbf{k}') \delta(\mathbf{k} - \mathbf{k}') \delta(\boldsymbol{\kappa} - \boldsymbol{\kappa}') d\mathbf{k}' d\mathbf{k} \\ &= \delta(\boldsymbol{\kappa} - \boldsymbol{\kappa}') \iint_{\mathcal{D}(\mathbf{k})} |\zeta(\mathbf{k})|^2 d\mathbf{k} = 2\pi k_0 \delta(\boldsymbol{\kappa} - \boldsymbol{\kappa}'). \end{aligned} \quad (\text{A1})$$

On this basis, we can calculate the autocorrelation of $\hat{H}_z(\kappa_z)$ as follows:

$$\begin{aligned} & \mathbb{E} \left\{ \hat{H}_z(\kappa_z) \hat{H}_z^*(\kappa'_z) \right\} \\ &= \int_{-\sqrt{k_0^2 - \kappa_z^2}}^{\sqrt{k_0^2 - \kappa_z^2}} \int_{-\sqrt{k_0^2 - \kappa_z'^2}}^{\sqrt{k_0^2 - \kappa_z'^2}} \frac{\mathbb{E} \left\{ \hat{H}(\boldsymbol{\kappa}) \hat{H}^*(\boldsymbol{\kappa}') \right\}}{\sqrt{\gamma(\kappa_x, \kappa_z) \gamma(\kappa'_x, \kappa'_z)}} d\kappa'_x d\kappa_x \\ &= 2\pi k_0 \int_{-\sqrt{k_0^2 - \kappa_z^2}}^{\sqrt{k_0^2 - \kappa_z^2}} \int_{-\sqrt{k_0^2 - \kappa_z'^2}}^{\sqrt{k_0^2 - \kappa_z'^2}} \frac{\delta(\kappa_x - \kappa'_x) \delta(\kappa_z - \kappa'_z)}{\sqrt{\gamma(\kappa_x, \kappa_z) \gamma(\kappa'_x, \kappa'_z)}} d\kappa'_x d\kappa_x \\ &= 2\pi k_0 \delta(\kappa_z - \kappa'_z) \int_{-\sqrt{k_0^2 - \kappa_z^2}}^{\sqrt{k_0^2 - \kappa_z^2}} \frac{1}{\sqrt{\gamma(\kappa_x, \kappa_z) \gamma(\kappa_x, \kappa'_z)}} d\kappa_x \\ &= 2\pi^2 k_0 \delta(\kappa_z - \kappa'_z). \end{aligned} \quad (\text{A2})$$

Finally, the autocorrelation function of $\hat{h}_c(z)$ can be calculated as follows:

$$\begin{aligned} R_c(z, z') &= \mathbb{E} \left\{ \hat{h}_c(z) \hat{h}_c^*(z') \right\} \\ &= \frac{A_s^2(k_0)}{16\pi^4} \int_{-k_0}^{k_0} \int_{-k_0}^{k_0} \mathbb{E} \left\{ \hat{H}_z(\kappa_z) \hat{H}_z^*(\kappa'_z) \right\} e^{j\kappa_z z} e^{-j\kappa'_z z'} d\kappa_z d\kappa'_z \\ &= \frac{1}{2k_0} \int_{-k_0}^{k_0} \int_{-k_0}^{k_0} \delta(\kappa_z - \kappa'_z) e^{j\kappa_z z} e^{-j\kappa'_z z'} d\kappa_z d\kappa'_z \\ &= \frac{1}{2k_0} \int_{-k_0}^{k_0} e^{j\kappa_z(z-z')} d\kappa_z = \frac{\sin(k_0(z-z'))}{k_0(z-z')}. \end{aligned} \quad (\text{A3})$$

B. Numerical Evaluation for Eigenvalues of $R_c(z, z')$

The characteristic equation for $R_c(z, z')$ is given by

$$\int_{\mathcal{Z}} R_c(z, z') \phi(z') dz' = \lambda \phi(z). \quad (\text{A4})$$

In order to discretize the integral, we use the Gauss-Legendre quadrature given as follows [31]:

$$\int_a^b f(x) dx \approx \frac{b-a}{2} \sum_{t=1}^T \omega_t f\left(\frac{b-a}{2} \eta_t + \frac{a+b}{2}\right), \quad (\text{A5})$$

where T is a complexity-vs-accuracy trade-off parameter, ω_t are the quadrature weights, and η_m are the roots of the T -th Legendre polynomial [31]. Accordingly, we have

$$\int_{\mathcal{Z}} R_c(z, z') \phi(z') dz' \approx \sum_{t=1}^T \frac{L_t}{2} \omega_t R_c(z, z_t) \phi(z_t) = \lambda \phi(z), \quad (\text{A6})$$

where $z_t = \frac{L_t \eta_t + d + L_t}{2}$ for $t \in \{1, \dots, T\}$. We also take z as the same set of nodes $\{z_{t'}\}_{t'=1}^T$, which yields

$$\sum_{t=1}^T \frac{L_t}{2} \omega_t R_c(z_{t'}, z_t) \phi(z_t) = \lambda \phi(z_{t'}). \quad (\text{A7})$$

This can be equivalently written as

$$\mathbf{Z} \boldsymbol{\phi} = \lambda \boldsymbol{\phi}, \quad (\text{A8})$$

where $[\mathbf{Z}]_{t',t} = \frac{L_t}{2} \omega_t R_c(z_{t'}, z_t)$, and $\boldsymbol{\phi} = [\phi(z_1), \dots, \phi(z_T)]^T$. Consequently, the eigenvalues of the matrix \mathbf{Z} are approximations of the eigenvalues of $R_c(z_{t'}, z_t)$, and the accuracy improves as T increases.

C. Proof of Lemma 2

Given $\Psi_n \sim \mathcal{CN}(0, 1)$ for $\forall n$, it is clear that $\sum_{n=1}^{\infty} \sqrt{\lambda_n} \phi_n(z) \Psi_n \triangleq \bar{h}(z)$ is a zero-mean Gaussian random field. The autocorrelation function of $\bar{h}(z)$ is given by

$$\begin{aligned} & \mathbb{E} \left\{ \bar{h}(z) \bar{h}^*(z') \right\} \\ &= \sum_{n=1}^{\infty} \sum_{n'=1}^{\infty} \sqrt{\lambda_n \lambda_{n'}} \phi_n(z) \phi_{n'}^*(z') \mathbb{E} \left\{ \Psi_n \Psi_{n'}^* \right\}. \end{aligned} \quad (\text{A9})$$

Since $\{\Psi_n\}_{n=1}^{\infty}$ are i.i.d. ZUCG, we have $E \left\{ \Psi_n \Psi_{n'}^* \right\} = \delta_{n,n'}$, which yields

$$E \left\{ \bar{h}(z) \bar{h}^*(z') \right\} = \sum_{n=1}^{\infty} \lambda_n \phi_n(z) \phi_n^*(z') = R_c(z, z'). \quad (\text{A10})$$

This means that $\bar{h}(z)$ also has the same autocorrelation with $\hat{h}_c(z)$, which completes the proof.

D. Proof of Theorem 1

The distance between the point $\mathbf{t} = [0, 0, z] \in \mathcal{A}_t$ and the target position $\mathbf{p}_s = [p_{s,x}, p_{s,y}, p_{s,z}]$ is given by

$$\|\mathbf{t} - \mathbf{p}_s\| = \sqrt{z^2 - 2p_{s,z}z + p_{s,x}^2 + p_{s,y}^2 + p_{s,z}^2}. \quad (\text{A11})$$

Therefore, the sensing link $h_s(\mathbf{t})$ can be expressed as follows:

$$h_s(\mathbf{t}) = \frac{e^{-jk_0 \sqrt{z^2 - 2p_{s,z}z + p_{s,x}^2 + p_{s,y}^2 + p_{s,z}^2}}}{\sqrt{4\pi(z^2 - 2p_{s,z}z + p_{s,x}^2 + p_{s,y}^2 + p_{s,z}^2)}} \triangleq \hat{h}_s(z). \quad (\text{A12})$$

As a result, we have

$$\int_{\mathcal{A}_t} |h_s(\mathbf{t})|^2 dt = \frac{1}{4\pi} \int_{d/2}^{d/2+L_t} \frac{1}{z^2 - 2p_{s,z}z + p_{s,x}^2 + p_{s,y}^2 + p_{s,z}^2} dz. \quad (\text{A13})$$

The above integral can be calculated with the aid of [30, Eq. (2.103.4)], which yields $\int_{\mathcal{A}_t} |h_s(\mathbf{t})|^2 dt = G_t$. Similarly, we can obtain $\int_{\mathcal{A}_r} |h_s(\mathbf{r})|^2 dr = G_r$. Inserting them into (48) gives (49).

E. Proof of Theorem 2 and 3

It is straightforward to show that $\rho \sim \mathcal{CN}(0, \Xi)$. Hence, $|\rho|^2$ follows an exponential distribution, i.e., $|\rho|^2 \sim \text{Exp}(\frac{1}{\Xi})$. Consequently, the ECR is calculated as

$$\overline{\mathcal{R}}_c^s = \int_0^\infty \log_2 \left(1 + \overline{\gamma}_c \frac{x}{\int_{\mathcal{A}_t} |h_s(\mathbf{t})|^2 dt} \right) \frac{1}{\Xi} e^{-\frac{x}{\Xi}} dx. \quad (\text{A14})$$

Inserting $\int_{\mathcal{A}_t} |h_s(\mathbf{t})|^2 dt = G_t$ into (A14) and using [30, (4.337.2)], the results of (54) can be derived.

The OP for the S-C design is calculated as

$$\begin{aligned} \mathcal{P}_s &= \Pr(\mathcal{R}_c^s < \mathcal{R}_0) \\ &= \Pr\left(|\rho|^2 < \frac{2^{\mathcal{R}_0} - 1}{\overline{\gamma}_c} \int_{\mathcal{A}_t} |h_s(\mathbf{t})|^2 dt\right) \\ &= F_\rho\left(\frac{2^{\mathcal{R}_0} - 1}{\overline{\gamma}_c} \int_{\mathcal{A}_t} |h_s(\mathbf{t})|^2 dt\right). \end{aligned} \quad (\text{A15})$$

Here, $F_\rho(x) = 1 - e^{-\frac{x}{\Xi}}$ is the cumulative distribution function (CDF) of $|\rho|^2$. The results of (57) then follows immediately.

F. Proof of Lemma 4

We can rewrite (69) as follows:

$$\mathcal{R}_s^c = \frac{1}{L} \log_2 \Delta - \frac{1}{L} \log_2 g_c, \quad (\text{A16})$$

where

$$\begin{aligned} \Delta &= \int_{\mathcal{Z}} |\hat{h}_c(z)|^2 dz + L\alpha_s \overline{\gamma}_s \int_{\mathcal{A}_r} |h_s(\mathbf{r})|^2 dr \left| \int_{\mathcal{Z}} \hat{h}_s(z) \hat{h}_c^*(z) dz \right|^2 \\ &= \int_{\mathcal{Z}} \int_{\mathcal{Z}} \hat{h}_c^*(z) (\delta(z - z') + \\ &\quad L\alpha_s \overline{\gamma}_s \int_{\mathcal{A}_r} |h_s(\mathbf{r})|^2 dr \hat{h}_s(z) \hat{h}_s^*(z')) \hat{h}_c(z') dz dz'. \end{aligned} \quad (\text{A17})$$

Furthermore, it is easily shown that $\hat{h}_c(z)$ can be written as $\hat{h}_c(z) = \int_{\mathcal{Z}} \tilde{R}_c(z, z_1) \bar{h}(z_1) dz_1$, where $\bar{h}(z) \sim \mathcal{CN}(0, 1)$ satisfies $\mathbb{E}\{\bar{h}(z) \bar{h}^*(z')\} = \delta(z - z')$. On this basis, Δ can be expressed as

$$\Delta = \int_{\mathcal{Z}} \int_{\mathcal{Z}} \bar{h}^*(z_1) Q(z_1, z_2) \bar{h}(z_2) dz_1 dz_2. \quad (\text{A18})$$

Substituting the eigendecomposition $Q(z_1, z_2) = \sum_{n=1}^\infty \nu_n \psi_n(z_1) \psi_n^*(z_2)$ into (A18) gives

$$\begin{aligned} \Delta &= \sum_{n=1}^\infty \nu_n \int_{\mathcal{Z}} \int_{\mathcal{Z}} \bar{h}^*(z_1) \psi_n(z_1) \psi_n^*(z_2) \bar{h}(z_2) dz_1 dz_2 \\ &= \sum_{n=1}^\infty \nu_n \left| \int_{\mathcal{Z}} \bar{h}^*(z) \psi_n(z) dz \right|^2. \end{aligned} \quad (\text{A19})$$

Since it is clear that $\int_{\mathcal{Z}} \bar{h}^*(z) \psi_n(z) dz$ is a ZUCG random variable, based on the Landau's eigenvalue theorem, we can write $\Delta = \sum_{n=1}^{\text{DoF}_Q} \nu_n |\Phi_n|^2$, which, together with (A16), leads to the results in Lemma 4.

G. Proof of Lemma 5

We prove Lemma 5 by contradiction. Assume that $w(\mathbf{t})$ does not lie in the subspace spanned by $\{h_s^*(\mathbf{t}), h_c^*(\mathbf{t})\}$. Under this assumption, $w(\mathbf{t})$ must contain a component that is orthogonal to both $h_s^*(\mathbf{t})$ and $h_c^*(\mathbf{t})$, which can be represented as follows:

$$w(\mathbf{t}) = \hat{w}(\mathbf{t}) + \hat{w}_\perp(\mathbf{t}), \quad (\text{A20})$$

where $\hat{w}(\mathbf{t}) = a h_s^*(\mathbf{t}) + b h_c^*(\mathbf{t})$ with $a, b \in \mathbb{C}$ is an arbitrary function that lies in the subspace spanned by $\{h_s^*(\mathbf{t}), h_c^*(\mathbf{t})\}$, while the term $\hat{w}_\perp(\mathbf{t})$ represents the orthogonal component that lies outside this subspace. Consequently, we can obtain

$$\Upsilon_s(w(\mathbf{t})) = \left| \int_{\mathcal{A}_t} h_s(\mathbf{t}) \hat{w}(\mathbf{t}) dt \right|^2 = \Upsilon_s(\hat{w}(\mathbf{t})), \quad (\text{A21a})$$

$$\Upsilon_c(w(\mathbf{t})) = \left| \int_{\mathcal{A}_t} h_c(\mathbf{t}) \hat{w}(\mathbf{t}) dt \right|^2 = \Upsilon_c(\hat{w}(\mathbf{t})). \quad (\text{A21b})$$

Additionally, the power constraint yields

$$\int_{\mathcal{A}_t} |w(\mathbf{t})|^2 dt = \int_{\mathcal{A}_t} |\hat{w}(\mathbf{t})|^2 dt + \int_{\mathcal{A}_t} |\hat{w}_\perp(\mathbf{t})|^2 dt. \quad (\text{A22})$$

From (A21) and (A22), it can be observed that the orthogonal component $\hat{w}_\perp(\mathbf{t})$ neither enhances SR nor CR, while it still consumes extra power. As $\hat{w}_\perp(\mathbf{t})$ provides no benefit to system performance but increases power usage, it should be eliminated. Consequently, the optimal beamformer can be expressed as $w(\mathbf{t}) = \hat{w}(\mathbf{t}) = a h_s^*(\mathbf{t}) + b h_c^*(\mathbf{t})$, which lies within the subspace spanned by $\{h_s^*(\mathbf{t}), h_c^*(\mathbf{t})\}$.

H. Proof of Lemma 6

The KKT conditions for problem (78) is given as follows:

$$\begin{aligned} \nabla(-\Upsilon) + \nu \nabla(\|\mathbf{w}\|^2 - 1) + \mu_1 \nabla(\tau \Upsilon - |\mathbf{h}_s^T \mathbf{w}|^2) \\ + \mu_2 \nabla((1 - \tau) \Upsilon - |\mathbf{h}_c^T \mathbf{w}|^2) = \mathbf{0}, \end{aligned} \quad (\text{A23})$$

$$\mu_1(\tau \Upsilon - |\mathbf{h}_s^T \mathbf{w}|^2) = 0, \quad (\text{A24})$$

$$\mu_2((1 - \tau) \Upsilon - |\mathbf{h}_c^T \mathbf{w}|^2) = 0, \quad (\text{A25})$$

$$\mu_1 \geq 0, \mu_2 \geq 0, \nu \in \mathbb{R}, \quad (\text{A26})$$

where ν, μ_1 , and μ_2 are real-valued Lagrangian multipliers. We can obtain from (A23) that

$$\tau \mu_1 + (1 - \tau) \mu_2 = 1, \quad (\text{A27})$$

$$(\mu_1 \mathbf{h}_s^* \mathbf{h}_s^T + \mu_2 \mathbf{h}_c^* \mathbf{h}_c^T) \mathbf{w} = \nu \mathbf{w}. \quad (\text{A28})$$

From (A27), it can be observed that μ_1 and μ_2 cannot both be zero at the same time. Hence, we analyze the problem under the following three possible cases.

1) $\mu_1 > 0$ and $\mu_2 = 0$: In this case, we can obtain from (A24) that $\Upsilon = \frac{|\mathbf{h}_s^* \mathbf{w}|^2}{\|\mathbf{h}_s\|^2}$. To maximize Υ , the optimal solution is $\mathbf{w}_\tau = \frac{\mathbf{h}_s^*}{\|\mathbf{h}_s\|} = \frac{\mathbf{h}_s^*}{\sqrt{G_t}}$, leading to $\Upsilon_* = \frac{G_t}{\tau}$. By substituting this into the constraint $|\mathbf{h}_c^T \mathbf{w}|^2 \geq (1 - \tau)\Upsilon$ gives the range $\tau \in \left[\frac{G_t^2}{G_t^2 + |\rho|^2}, 1 \right]$.

2) $\mu_1 = 0$ and $\mu_2 > 0$: By following the same procedure as in above case, we derive $\mathbf{w}_\tau = \frac{\mathbf{h}_c^*}{\sqrt{g_c}}$ with $\tau \in \left[0, \frac{|\rho|^2}{|\rho|^2 + g_c^2} \right]$.

3) $\mu_1 > 0$ and $\mu_2 > 0$: From (A24) and (A25), we have

$$\Upsilon = \frac{1}{\tau} |\mathbf{h}_s^T \mathbf{w}|^2 = \frac{1}{1 - \tau} |\mathbf{h}_c^T \mathbf{w}|^2. \quad (\text{A29})$$

Based on (A28), \mathbf{w} can be expressed as a linear combination of \mathbf{h}_s and \mathbf{h}_c :

$$\mathbf{w} = \frac{\mu_1 \mathbf{h}_s^T \mathbf{w}}{\nu} \mathbf{h}_s^* + \frac{\mu_2 \mathbf{h}_c^T \mathbf{w}}{\nu} \mathbf{h}_c^* \triangleq \alpha \mathbf{h}_s^* + \beta \mathbf{h}_c^*. \quad (\text{A30})$$

Subsequently, from (A29), we can obtain

$$\frac{\alpha}{\beta} = \frac{\mu_1 \sqrt{\tau}}{\mu_2 \sqrt{1 - \tau} e^{-j\angle \rho}}. \quad (\text{A31})$$

Substituting (A30) into (A28) gives

$$\mu_1 (G_t + \rho \beta / \alpha) = \mu_2 (g_c + \rho^* \alpha / \beta) = \nu, \quad (\text{A32})$$

which, together with (A27) and (A31), yields

$$\mu_1 = \frac{g_c - \sqrt{(1 - \tau)/\tau} |\rho|}{(1 - \tau)G_t + \tau g_c - 2\sqrt{\tau(1 - \tau)} |\rho|}, \quad (\text{A33})$$

$$\mu_2 = \frac{G_t - \sqrt{\tau/(1 - \tau)} |\rho|}{(1 - \tau)G_t + \tau g_c - 2\sqrt{\tau(1 - \tau)} |\rho|}. \quad (\text{A34})$$

Under the conditions $\mu_1 > 0$ and $\mu_2 > 0$, τ should satisfies $\tau \in \left(\frac{|\rho|^2}{|\rho|^2 + G_t^2}, \frac{g_c^2}{g_c^2 + |\rho|^2} \right)$. According to (A31), the optimal \mathbf{w} in this scenario can be formulated as follows:

$$\mathbf{w}_\tau = \frac{\mu_1 \sqrt{\tau}}{\varsigma} \mathbf{h}_s^* + \frac{\mu_2 \sqrt{1 - \tau} e^{-j\angle \rho}}{\varsigma} \mathbf{h}_c^*, \quad (\text{A35})$$

where ς is for normalization. Taken together, the proof of Lemma 6 is completed.

REFERENCES

- [1] F. Liu, Y. Cui, C. Masouros, J. Xu, T. X. Han, Y. C. Eldar, and S. Buzzi, "Integrated sensing and communications: Toward dual-functional wireless networks for 6G and beyond," *IEEE J. Sel. Areas Commun.*, vol. 40, no. 6, pp. 1728–1767, Jun. 2022.
- [2] A. Liu *et al.*, "A survey on fundamental limits of integrated sensing and communication," *IEEE Commun. Surveys Tuts.*, vol. 24, no. 2, pp. 994–1034, Feb. 2022.
- [3] C. Ouyang, Y. Liu, H. Yang, and N. Al-Dahir, "Integrated sensing and communications: A mutual information-based framework," *IEEE Commun. Mag.*, vol. 61, no. 5, pp. 26–32, May 2023.
- [4] L. Xie, F. Liu, J. Luo, and S. Song, "Sensing mutual information with random signals in Gaussian channels," *IEEE Trans. Commun.*, vol. 73, no. 10, pp. 9437–9452, Oct. 2025.
- [5] Y. Liu, C. Ouyang, Z. Wang, J. Xu, X. Mu, and Z. Ding, "CAPA: Continuous-aperture arrays for revolutionizing 6G wireless communications," *IEEE Wireless Commun.*, vol. 32, no. 4, pp. 38–45, Aug. 2025.
- [6] A. S. Poon, R. W. Brodersen, and D. N. Tse, "Degrees of freedom in multiple-antenna channels: A signal space approach," *IEEE Trans. Inf. Theory*, vol. 51, no. 2, pp. 523–536, Feb. 2005.
- [7] A. Pizzo, A. de Jesus Torres, L. Sanguinetti, and T. L. Marzetta, "Nyquist sampling and degrees of freedom of electromagnetic fields," *IEEE Trans. Signal Process.*, vol. 70, pp. 3935–3947, 2022.
- [8] D. Dardari, "Communicating with large intelligent surfaces: Fundamental limits and models," *IEEE J. Sel. Areas Commun.*, vol. 38, no. 11, pp. 2526–2537, Nov. 2020.
- [9] A. Pizzo, L. Sanguinetti, and T. L. Marzetta, "Spatial characterization of electromagnetic random channels," *IEEE Open J. Commun. Soc.*, vol. 3, pp. 847–866, 2022.
- [10] Z. Wan, J. Zhu, and L. Dai, "Can continuous aperture MIMO obtain more mutual information than discrete MIMO?" *IEEE Commun. Lett.*, vol. 27, no. 12, pp. 3185–3189, Dec. 2023.
- [11] B. Zhao, C. Ouyang, X. Zhang, and Y. Liu, "Continuous aperture array (CAPA)-based wireless communications: Capacity characterization," *IEEE Trans. Wireless Commun.*, vol. 24, no. 12, pp. 10456–10473, 2025.
- [12] C. Ouyang, Z. Wang, X. Zhang, and Y. Liu, "Diversity and multiplexing for continuous aperture array (CAPA)-based communications," *IEEE Trans. Wireless Commun.*, vol. 24, no. 10, pp. 8662–8680, 2025.
- [13] Z. Zhang and L. Dai, "Pattern-division multiplexing for multi-user continuous-aperture MIMO," *IEEE J. Sel. Areas Commun.*, vol. 41, no. 8, pp. 2350–2366, Aug. 2023.
- [14] M. Qian, L. You, X.-G. Xia, and X. Gao, "On the spectral efficiency of multi-user holographic MIMO uplink transmission," *IEEE Trans. Wireless Commun.*, vol. 23, no. 10, pp. 15421–15434, Oct. 2024.
- [15] Z. Wang, C. Ouyang, and Y. Liu, "Optimal beamforming for multi-user continuous aperture array (CAPA) systems," *IEEE Trans. Commun.*, vol. 73, no. 10, pp. 9207–9221, Oct. 2025.
- [16] —, "Beamforming optimization for continuous aperture array (CAPA)-based communications," *IEEE Trans. Wireless Commun.*, vol. 24, no. 6, pp. 5099–5113, 2025.
- [17] M. Qian, X. Mu, L. You, and M. Matthaiou, "Continuous aperture array (CAPA)-based multi-group multicast communications," *IEEE Trans. Commun.*, vol. 74, pp. 3787–3801, Jan. 2026.
- [18] S. Chen, J. Guo, and S. Han, "Implicit neural representation of beamforming for continuous aperture array (CAPA) system," *arXiv preprint arXiv:2507.03609*, 2025.
- [19] A. Chen, L. Chen, Y. Chen, C. You, G. Wei, and F. R. Yu, "Cramér-Rao bounds of near-field positioning based on electromagnetic propagation model," *IEEE Trans. Veh. Technol.*, vol. 72, no. 11, pp. 13808–13825, Nov. 2023.
- [20] A. Chen, L. Chen, Y. Chen, N. Zhao, and C. You, "Near-field positioning and attitude sensing based on electromagnetic propagation modeling," *IEEE J. Sel. Areas Commun.*, vol. 42, no. 9, pp. 2179–2195, Sep. 2024.
- [21] H. Jiang, Z. Wang, Y. Liu, and A. Nallanathan, "Cramér-Rao bounds optimization for near-field sensing with continuous-aperture arrays," *IEEE Trans. Wireless Commun.*, vol. 25, pp. 7032–7047, 2026.
- [22] B. Zhao, C. Ouyang, X. Zhang, H. Shin, and Y. Liu, "Downlink and uplink ISAC in continuous-aperture array (CAPA) systems," *IEEE Trans. Wireless Commun.*, vol. 25, pp. 3592–3609, 2026.
- [23] Y. Zhang *et al.*, "Exploiting continuous-aperture arrays in integrated sensing and communication systems," *IEEE Trans. Wireless Commun.*, vol. 24, no. 11, pp. 9539–9555, Nov. 2025.
- [24] C. Ouyang, Z. Wang, B. Zhao, X. Zhang, and Y. Liu, "On the impact of reactive region on the near-field channel gain," *IEEE Commun. Lett.*, vol. 28, no. 10, pp. 2417–2421, Oct. 2024.
- [25] T. Zwick, C. Fischer, and W. Wiesbeck, "A stochastic multipath channel model including path directions for indoor environments," *IEEE J. Sel. Areas Commun.*, vol. 20, no. 6, pp. 1178–1192, Aug. 2002.
- [26] M. A. Richards, *Fundamentals of Radar Signal Processing*. New York, NY, USA: McGraw-Hill Educ., 2014.
- [27] H. J. Landau and H. Widom, "Eigenvalue distribution of time and frequency limiting," *J. Math. Anal. and Appl.*, vol. 77, no. 2, pp. 469–481, 1980.
- [28] M. Franceschetti, "On landau's eigenvalue theorem and information cut-sets," *IEEE Trans. Inf. Theory*, vol. 61, no. 9, pp. 5042–5051, Sep. 2015.
- [29] P. G. Moschopoulos, "The distribution of the sum of independent gamma random variables," *Ann. Inst. Statist. Math.*, vol. 37, no. 1, pp. 541–544, 1985.
- [30] I. S. Gradshteyn and I. M. Ryzhik, *Table of Integrals, Series and Products*, 7th ed. New York, NY, USA: Academic Press, 2007.
- [31] F. W. Olver, D. W. Lozier, R. F. Boisvert, and C. W. Clark, *NIST Handbook of Mathematical Functions*. Cambridge, U.K.: Cambridge univ. press, 2010.